

VARIATION IN COAL COMPOSITION

A computational approach to study the mineral
composition of individual coal particles

O. Charon, S. G. Kang, K. Graham, A. F. Sarofim and J. M. Beer

Department of Chemical Engineering
Massachusetts Institute of Technology
Cambridge, MA 02139 (U.S.A.)

Mineral matter transformations, and therefore fly ash evolution, during pulverized coal combustion depend on the amount, composition and spatial distribution of the inorganic matter within individual pulverized coal particles. Thus, it is necessary to have information on the mineral composition of individual particles, as well as that of the raw pulverized coal. A model has been developed to predict the variation of individual coal particle compositions. It uses CCSEM data for a given raw coal as input and randomly distributes the mineral inclusions in the coal volume. By random selection of monosize coal particles, it is possible to generate distributions of mineral content for any particle size distribution of coal. The model has been checked by comparing computed results with data on the compositional variations of narrowly size and density classified fractions of an Upper Freeport bituminous coal. The results for individual coal particle compositions are used to generate information on the variability of the composition of the fly ash generated during combustion.

1. INTRODUCTION

Understanding the processes that govern the size distribution and chemical composition of the ash within and at the exit of a pulverized coal fired combustor is important because the ash influences fouling, slagging, and heat transfer in boilers, as well as the downstream particulate control equipment. This understanding begins with not only a knowledge of the amount, composition, and spatial distribution of the mineral matter in the coal particles, but also with some knowledge of the variability of the mineral content of the coal particles.

In this paper a model is presented for calculating the distribution of mineral inclusions in pulverized coal of different size and density fractions from knowledge of the mineral inclusions in the parent coal. A test of the validity of the model is provided by comparing the model predictions of the variations in the composition of different size and density fractions of an Upper Freeport coal with computer controlled scanning electron microscopy (CCSEM) measurements of the mineral distributions. The results obtained for the Upper Freeport coal show good agreement between the CCSEM data and the model results, and also give information on the variation of individual coal particle compositions.

This study is part of a broader program on mineral matter transformations being funded by the DOE and coordinated by Physical Sciences Inc. The coal classification was done by Foster Wheeler and the CCSEM analysis by Huffman and Huggins at the University of Kentucky. The results of this study will be used as input into a model of char combustion which allows for coalescence of the mineral inclusions and fragmentation of the char in order to predict the composition and size of the fly ash.

2. EXPERIMENTAL

CCSEM analysis was performed on the Upper Freeport raw coal and several size and density fractions (63-105 μm , and less than 1.3 , 1.3 - 1.8 , 1.8 - 2.85 , and greater than 2.85 g/cm^3) by Huffman and Huggins at the University of Kentucky. The CCSEM analysis provides the content and size distribution of each of the mineral species listed in Table 1. For details on the CCSEM analysis used to obtain these data, one can consult the publications of these two specialists [2][3][4], as well as other authors [5][6].

The main mineral species in the Upper Freeport raw coal are, by decreasing amount, Illite, Mixed silicates, Pyrite, Quartz and Kaolinite. All the other species occur in concentrations less than 2 wt%. The CCSEM gives the mineral inclusion size distribution for these five main mineral types and for the total minerals (Table 1). For the latter, all the sizes are equally represented in the range from 10 to 15%, except the largest size (greater than 40 μm) which reaches 36%.

The CCSEM data obtained for the Upper Freeport raw coal were used as input to the model. The CCSEM data obtained for the four size and density classified samples were compared with computed values in order to validate the model.

3. MODEL

The model has two objectives : first, it must simulate a raw coal volume with different types and sizes of mineral inclusions inside, and second, it must produce coal particles from this computed raw coal volume, sort them by density, and perform statistics on them. To accomplish these objectives two Fortran programs were created : Pr1 and Pr2.

The major difficulty in simulating the raw coal volume is storing the information about the mineral inclusions (type, size, location...) and about the coal particles (mineral composition, density...) during the run. In the case of the Upper Freeport coal, greater than five million inclusions must be stored in order to get at least one mineral inclusion for each type and size. Only a super computer has sufficient memory to handle all of this information. We used an IBM 3090-600E with 512 megabytes of real memory and 512 megabytes of expended storage.

3.1 Raw coal volume simulation (Pr1)

3.1.1 Definitions

The raw coal volume is cubic and divided into a cubic matrix with unit length of one micron. The mineral inclusions are assumed to be cubic and are assigned to occupy sites within the raw coal matrix. Eventually the coal matrix is divided into smaller cubes which are coal particles.

The model assumes 6 different possible mineral inclusion sizes, one average size for each size range given by the CCSEM analysis. These sizes are defined using an integer number I from 1 to 6 and the D (I) values are, respectively, 1, 4, 8, 16, 30, and 60 μm .

The model accounts for the five main mineral species of the Upper Freeport raw coal as defined by the CCSEM analysis (4) (see Table 1), and identifies them by an integer number J. To achieve a mineral mass balance, a sixth kind of mineral, called "Other", is defined. The "other" content, composition and size distribution are calculated to fit the total mineral inclusion analysis given by the CCSEM data :

$$f_m(6) = 1 - \sum_{J=1}^5 f_m(J) \quad \text{and}$$

$$f_{m,s}(6, I) = 1 / f_m(6) \cdot [f_{m,s}(\text{All mineral}, I) - \sum_{J=1}^5 f_m(J) \cdot f_{m,s}(J, I)] \quad \text{with}$$

$$f_{m,s}(\text{All mineral}, I) = \sum_{J=1}^6 f_{m,s}(J, I)$$

where $f_m(J)$ is the mass fraction of the mineral J in all mineral
and $f_{m,s}(J, I)$ is the mass fraction of the size I for mineral J.

The last species to be defined is the mineral free coal (J=0). The density of this last species is an input data for the model and depends on the raw coal studied. A value of 1.2 g/cm³ was assumed for the Upper Freeport coal.

3.1.2 Random location of the mineral inclusions

An inclusion is defined by the location (X_i, Y_i, Z_i) of its closest point to the origin of the raw coal volume, and by its size $D(1)$. X_i, Y_i, Z_i are randomly computed between 0 and $L - D(1)$, where L is the size of the simulated raw coal cube.

In order to avoid overlap between two mineral inclusions, all of the sites used by a mineral inclusion are recorded. Then if a latter inclusion needs to use one of these recorded sites for its location, its location is randomly computed again. This test is necessary to avoid inclusion overlap, particularly for the Upper Freeport (20.5 wt% of mineral matter) where almost 10% of its sites are mineral sites, but at a cost of a significant increase in run time and memory requirement.

3.1.3 Mineral inclusion attribution to a coal particle

Knowing $L, X_i, Y_i, Z_i, D(1)$ and the coal particle size (N_{spart}) which is to be created from the raw coal volume, it is possible to attribute a given mineral inclusion to a coal particle. The coal particles and mineral inclusions are identified as a function of their location in the raw coal cube by a characteristic integer given as :

$$\text{Num} = \left[\sum_{k=1}^3 \text{INT} \left((\text{Loc}(k) + D(1)/2) / N_{\text{spart}} \right) \cdot N_{\text{step}}^k \right] + 1$$

where $\text{Loc}(k)$ for $k=1$ to 3 are X_i, Y_i , and Z_i , respectively,
 $L = N_{\text{step}} \cdot N_{\text{spart}}$,
 and $\text{INT}(\text{value})$ is the integer part of value.

All the inclusions within a coal particle will have the same identifying integer, Num, as the coal particle. A coal particle will be allowed to contain a mineral inclusion if its size is greater than the inclusion size, if it contains the gravity center of the inclusion, and if there is enough remaining space for the additional inclusion. If a mineral inclusion is not in a coal particle, it is a pure mineral particle, keeping the former inclusion size; however, this case was never encountered for the 84 μm Upper Freeport coal.

3.1.4 Running Pr1

All of the illustrations in this presentation are given for the Upper Freeport raw coal and its four well classified samples, previously described. Because the model is at this time only able to produce a monosize coal sample, the results from the model will be given for the size 84 μm , which is an average value for the experimental sample size range 63 - 105 μm . The input file for a run consists of the CCSEM data for a given raw coal, chosen coal particle size and chosen particle number. Typically, the Pr1 run time was 14'27" CPU, and 350 megabytes of virtual memory was used to produce 5 100 981 mineral inclusions randomly distributed in a raw coal volume 840 μm large. As shown in Table 2, for a small number of biggest inclusions (only 2 for the quartz) we obtain an increasing number of inclusions when the inclusion size decreases, to finally reach 4 994 227 inclusions of 1 μm (98% of the total number). This is a problem with this computation : i.e., the biggest mineral inclusion size is not statistically well-defined, and we are too close to the maximum of memory available, to increase the number of inclusions.

The number of inclusion (N_{inc}) for a given mineral type J and a size I is calculated as follows :

$$N_{\text{inc}}(J, I) = \text{INT} \left[(V(J, I) / D(1)^3) + 0.5 \right]$$

where $V(J, I)$ is the volume used in the raw coal cube by the mineral J , calculated from the CCSEM data. In this way the difference between the computed and the measured coal sample mineral composition is always less than 0.1 wt% and the total mineral content is exactly the desired value of 20.5 wt%.

3.2 Coal particle characterization (Pr2)

Each individual coal particle is identified by an integer number, Num. Pr2 then calculates, for all the computed inclusions, the amount of mineral inclusion J with the size I which falls in the coal particle Num. All this information is stored and used to calculate the mineral content and composition, mass or density of every individual

coal particle. A density classification is achieved and any kind of statistical analysis is possible for the whole computed coal sample or any well classified size and density fraction.

The mineral inclusion listing and a parameter listing (L, Nstep, Npart, D (I)...) generated by Pr1 are the two input files necessary to run Pr2. Typically the run time was 2'15" CPU and 160 megabytes of virtual memory was used to produce 1000 particles of 84 μm .

4 Results

4.1 Model validation

Comparison of experimental CCSEM data for density classified Upper Freeport coal to model predictions is shown in Figure 1. Figure 1 shows good agreement for the mass distribution between the four density ranges and for the total mineral content in each density range. The fourth density range, where .2 wt% of the whole sample and a total mineral content of 91.6 wt% was calculated, does not give satisfactory agreement, but the reason becomes clear from an examination of the particle statistics in each density range. Whereas 516, 399, and 84 coal particles were obtained in the first, second and third density ranges, respectively, only one ended up in the fourth density range. Thus, the current model is limited by the large amount of memory necessary for a run and the fourth density range sample is too small to give representative results.

Good agreement for the mineral composition in the first two density ranges was also obtained (Figure 1), but for the same reason the last two ranges show disagreements. Even though the agreement is not good in the last two density ranges, the results do agree with the CCSEM data that the pyrite is the main mineral in particle greater than 2.85 g/cm³. The mineral composition cannot be statistically well determined because the sample size of the simulated biggest mineral inclusions is too small.

A new statistical approach is currently under development to reduce the representation of the smallest inclusion size (currently 98 % of the memory used by Pr1).

4.2 Individual coal particle information

Assuming the model is validated, we can study the mineral composition variation in individual coal particles. The results, obtained for the Upper Freeport, show as expected that the density classification provides coal samples with small variations in the total mineral content of individual particles (Figure 2). From the whole sample, which contains 18.08 wt% mineral matter per particle with a standard deviation of 15.20 wt%, we obtain four density classified samples, which contain 10.16, 18.40, 64.40 and 91.60 wt% of mineral matter per particle but with a standard deviation always less than 5 wt% (only 1.47 % for the first density range).

From an examination of the mineral composition of an individual coal particle (Figure 3), it appears that the fraction of a given mineral varies greatly even through the mean value does not (32 wt% for illite); the standard deviation, more over increases when the particle density increases (8.93, 18.90, and 49.5 wt% for the first, second and third density ranges, respectively). Denser coal particles contain larger inclusions, which because of their size they represent most of the mineral mass of that coal particle. This is why the mineral composition approaches the limit of either 0 or 100 wt% for a given mineral, when the particle density increases. Table 3 shows variations in compositions of a given mineral in individual particles. For the first and second density ranges the variation ranges are around 40 and 70%, respectively.

We also observed that the classified sample that is most representative of the whole coal sample is in the second density range (1.3 to 1.8 g/cm³).

5 conclusion

This new computational approach allows information to be obtained information on the mineral composition variation in individual coal particles, which can be useful for predicting the mineral transformations and the final fly ash size distribution during pulverized coal combustion. Without using sophisticated and expensive experiments, it is possible to obtain data on any classified samples and to compare them with fly ash composition. This information will be used as input to a model of coal particle combustion. This model can also be used to design a process for preparation of a well classified coal sample with a given mineral composition.

A future improvement of the model will be to develop a new statistical approach in which will increase the number of simulated big inclusions and reduced the memory required. This will allow for the characterization of the large particle composition variations as well.

Acknowledgement

We greatly acknowledge the support of DOE grant RA22-86PC90751 which made this work possible.

References

- [1] A. F. Sarofim , Polutant formation and destruction, Fundamental of the Physical-chemistry of pulverized coal combustion, J. Lahaye and G. Prado Ed., NATO ASI Series E, n°137, Nijhoff, 1987
- [2] G. P. Huffman and F. E. Huggins , Analysis of inorganic constituents in low rank coal, The Chemistry of Low Rank Coal, H. H. Schobert Ed., ACS Advances in Chemistry Series, American Chem. Soc., Washington D.C., pp 159-174, 1984
- [3] G. P. Huffman, F. E. Huggins and R. J. Lee, Scanning electron microscopy based automated analysis (SEM-AIA) and Mossbauer spectroscopy : Quantitative Characterization of Coal Minerals, Coal and Coal Products, Analytical Characterization Techniques, E. L. Fuller Jr, American Chem. Soc., ACS Symposium Series, Vol. 205, Washington D.C., pp 239-258, 1982
- [4] F. E. Huggins, D. A. Kosmack, G. P. Huffman and R. J. Lee, Coal Mineralogies by SEM Automated Image Analysis, Scanning Electron Microscopy, Vol. 1, pp 531-540, 1980
- [5] A. K. Moza, D. W. Sticker and L. G. Austin, Elemental analysis of Upper Freeport coal particles, Scanning Electron Microscopy, Vol. IV, pp 91-96, 1980
- [6] R. J. Lee and J. F. Kelly, overview of SEM-based automated image analysis, Scanning Electron Microscopy, Vol. 1, pp 303-310, 1980
- [7] H. Gan, S. P. Nandi and P. L. Walker, Nature of the porosity in american coal, Fuel, Vol. 51, pp 272-277, 1972
- [8] E. Raask, Mineral Impurities in Coal, Hemisphere Pub. Corp., 1985
- [9] O. P. Mahajan, Coal porosity, Coal Structure, R. A. Mayers Ed., Academic press, pp 51-86, 1982
- [10] J. J. Renton, Mineral matter in coal, Coal Structure, R. A. Mayers Ed., Academic press, pp 283-324, 1982

Table 1 : CCSEM data from J. Huffman and F. Huggins for the Upper Freeport raw coal

mineral	Wt% mineral matter	Size distribution (wt%)					
		<2.5µm	2.5-5µm	5-10µm	10-20µm	20-40µm	>40µm
Quartz	10	8	14	26	20	26	6
Kaolinite	7	15	9	15	25	19	16
Illite	35	10	10	13	11	12	44
Mix.il.	19	12	16	15	21	12	23
Pyrite	18	4	2	13	13	14	54
All mine.	100	9	10	15	15	14	36

Table 2 : Number of mineral inclusion in 1 mm³ of the raw Upper Freeport coal based on an average size, in each CCSEM analysis size range

Mineral	Number of inclusions					
	1 µm	4 µm	8 µm	16 µm	30 µm	60 µm
Quartz	503988	13781	3199	308	61	2
Kaolinite	604460	5667	1181	246	28	3
Illite	2014867	31482	5116	541	90	41
Mix. sil.	1268790	26433	3098	542	47	12
Pyrite	240402	1878	1526	191	31	15
Others	361720	9304	1750	145	22	14

Table 3 : Particle by particle mineral composition variations for two density classified samples of an 84 µm Upper Freeport coal (wt%)

	Range 1 : less than 1.3 g/cm ³				Range 2 : 1.3 to 1.8 g/cm ³			
	Mean	St. dev.	Min.	Max.	Mean	St. dev.	Min.	Max.
Particle number	516	-	-	-	399	-	-	-
Total mineral content	10.2	1.5	6.3	13.0	18.41	4.85	12.1	38.2
Mineral composition								
Quartz	14.8	7.3	3.2	46.8	15.1	16.0	1.5	69.5
Kaolinite	9.1	6.8	2.2	38.8	9.1	12.4	0.5	76.4
Illite	32.1	8.9	12.9	59.1	30.8	18.9	5.3	79.4
Mixed silicates	25.5	9.3	7.2	57.6	21.9	16.7	3.2	75.3
Pyrite	9.4	7.2	1.3	38.9	14.7	17.2	0.5	82.0
Others	9.1	5.5	1.8	32.9	8.4	11.4	0.9	64.0

Figure 1: Comparison between experimental data and model results for an 84 μm Upper Freeport raw coal sample

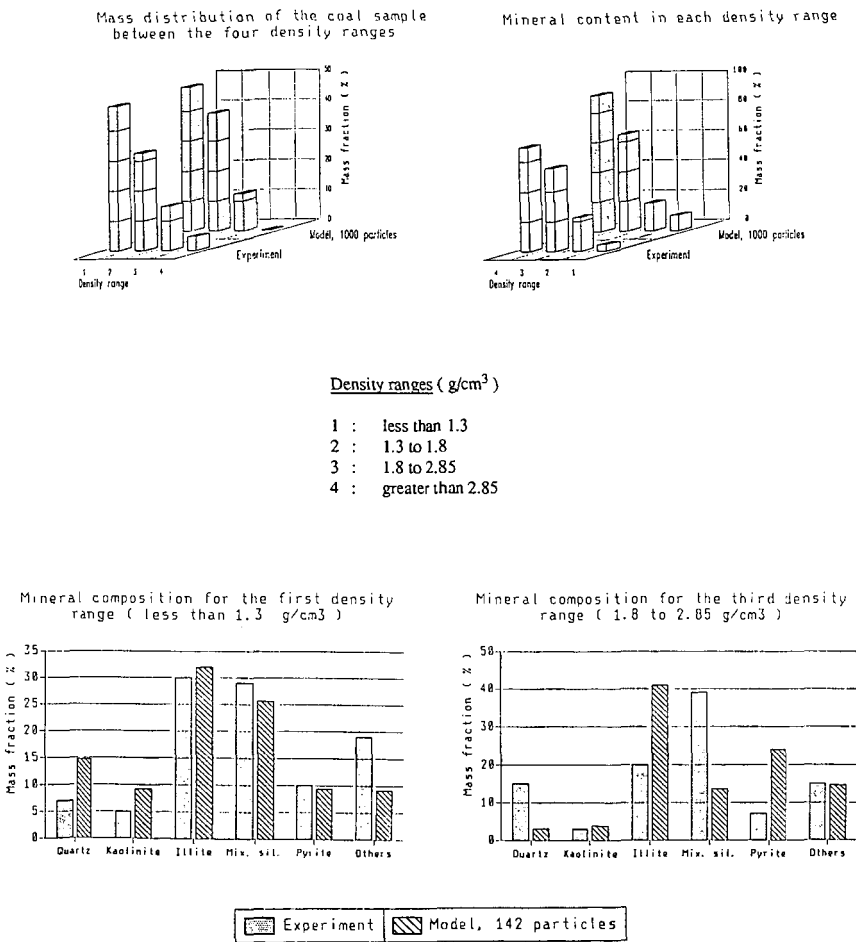


Figure 2: Model predictions of the total mineral content in different density classes for na 84 μ m Upper Freeport coal sample

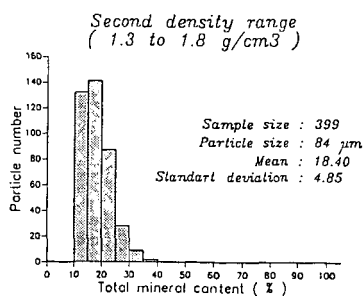
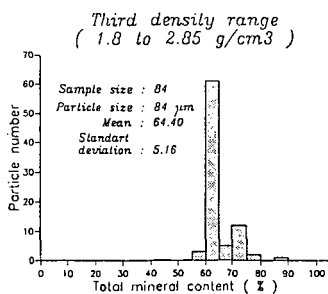
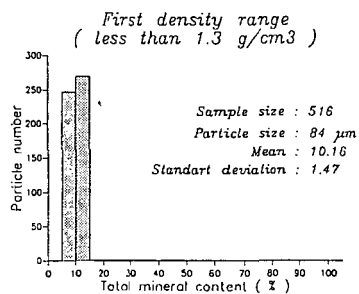
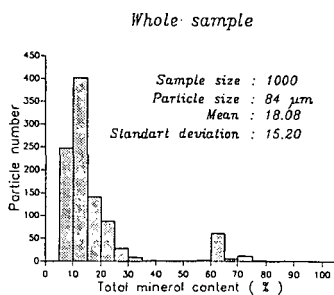
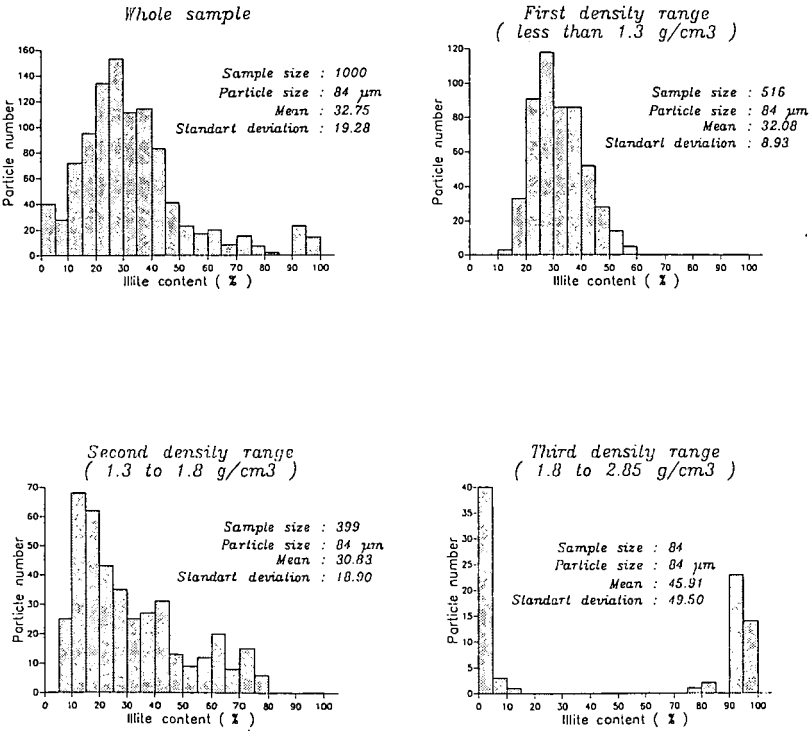


Figure 3 : Model predictions of the illite content in different density classes for an 84 μm Upper Freeport coal sample



NEW TECHNIQUES FOR THERMOCHEMICAL PHASE EQUILIBRIUM PREDICTIONS IN COAL ASH SYSTEMS

M. Ramanathan, S. Ness, D. Kalmanovitch

University of North Dakota
Energy and Mineral Research Center
Grand Forks, North Dakota 58202

ABSTRACT

PHOEBE is a new computer code developed at UNDEMRC as a part of a long-term study of coal ash deposition phenomena in combustion systems. The task of developing a new code was undertaken to eliminate the various problems encountered with existing phase equilibrium codes such as SOLGASMIX and PACKAGE. These codes were not able to produce satisfactory comparisons with experimental data and the goal of PHOEBE was to apply better techniques to calculate the minimum Gibbs free energy at thermodynamic equilibrium. The new PHOEBE algorithm has been rigorously tested against standard mathematical functions and is currently being tested against experimental data on coal ash slags. This paper discusses the minimization and optimization techniques used in PHOEBE.

I. Introduction

Understanding the behavior of inorganic constituents during coal combustion is needed to predict the development of ash deposit formation, slagging, and fouling in a combustor. This requires information on the formation of the various mineralogical phases in the vapor, liquid, and solid states and their relationship to the relative amounts of the inorganic elements present in the raw coal and to the variations in combustion conditions. With this type of data, a better understanding of not only the deposition processes but their mitigational aspects as well may be achieved. The calculation of the equilibrium species and phase distributions provides a good starting point in approximating the requisite data.

The problem of obtaining the equilibrium values (x^*_1, \dots, x^*_n) of n distinct species comprising a thermodynamic system S at a fixed temperature and pressure has been extensively addressed in the past, and the utility of obtaining the equilibrium values by minimizing the Gibbs free energy of the system has also been thoroughly emphasized (1-10). A variety of numerical packages (HALTAFALL, SOLGASMIX, PACKAGE, SHIMPO-GOTO, NASA-CEC, etc.,) related to this problem have been reported in the literature and their relative merits also discussed. Although the majority of these packages seem to perform adequately on many test cases, they sometimes also appear to produce quite erroneous results. (It must be pointed out that our experience with the above-mentioned packages is limited primarily to SOLGASMIX.) This is not unexpected, since conventionally, the calculations are simplified to the extent that the various interaction terms in the Gibbs free energy of the system are represented only by the 'free energy of mixing' terms, all other interactions being assumed minimal or nonexistent. It has been argued very convincingly that it is indeed valid to approximate the activities of the species by their respective mole fractions (11-13). Nonetheless, this minimality assumption has important consequences for the stability (and hence the existence) of various phases within the

system: even the introduction of a simple Lennard-Jones type potential in a non-interactive system, it may be recalled, lowers the energy of the system, favors the formation of the liquid phase, and would perhaps be more representative of the correct free energy of the system.

This in turn leads to the problem of the availability, or lack thereof, of thermochemical data. The most widely referred sources of thermodynamic data (16-18) often lack data for many of the typical products in coal combustion systems. It is to be also noted that the available thermodynamic tables are themselves extrapolated so that further extrapolations to unreferenced compounds may lead to additional sources of error.

The organization of the paper then is as follows. In Section II the mass constrained Gibbs free energy minimization problem is discussed in detail. A variety of standard numerical methods currently available and their relative merits are also briefly discussed. Section III describes PHOEBE, a Gibbs free energy minimization program currently under development at UNDEMRC.

II. Mass-Constrained Gibbs Free Energy Minimization

Let S be a multicomponent thermodynamic system at a given temperature T and pressure P comprising the species X^1, \dots, X^n and let G be Gibbs free energy of S . Let

$$A^{\alpha}_{aj} x^j_{\alpha} = b_a \quad 1)$$

be the mass constraint relations for S where

A^{α}_{aj} = stoichiometry coefficient of atom (or element) a in species j in phase α ,

x^j_{α} = the number of moles of species j in phase α ,

b_a = the number of moles of atom (or element) a .

In Equation 1 the index α ranges from 1 through the number of phases N_p , the index j ranges from 1 through the number of species N_s , and the index a ranges from 1 through the number of atoms or elements N_a . The Einstein summation convention is used in Equation 1 and in the rest of the paper. Implicit in Equation 1 are the nonnegativity requirements,

$$x^j_{\alpha} \geq 0, \quad 1 \leq j \leq N_s, \quad 1 \leq \alpha \leq N_p, \quad 2)$$

that need to be satisfied by the molar amounts of the various species in the system. The Gibbs free energy of S is written as

$$G = \sum_{\alpha} \sum_j x^j_{\alpha} \mu^{\alpha}_j \quad 3)$$

where the μ^{α}_j are the chemical potentials of the species which are in turn approximated as follows: let,

$$x_{\alpha} = \sum_{j=1}^{N_s} x_{j\alpha} \quad 4)$$

be the total number of moles in phase α , and $(\mu_o)^{\alpha_j}$ the standard chemical potential of species j in phase α . μ^{α_j} is then given by

$$\mu^{\alpha_j} = \left\{ \begin{array}{ll} x_{j\alpha}(\mu_o)^{\alpha_j} & , \text{ if } \alpha \text{ is a pure condensed phase} \\ x_{j\alpha}(\mu_o)^{\alpha_j} + x_{j\alpha} \ln \left[\frac{P x_{j\alpha}}{x_{\alpha}} \right] & , \text{ if } \alpha \text{ is a gas phase} \\ x_{j\alpha}(\mu_o)^{\alpha_j} + x_{j\alpha} \ln \left[\frac{x_{j\alpha}}{x_{\alpha}} \right] & , \text{ if } \alpha \text{ is a solid-liquid mixture} \end{array} \right\} \quad 5)$$

Note that, in Equation 5 the indices α and j are free indices and all implied summations over α and j are to be disabled.

Equations 3-5 approximating the Gibbs free energy of the system are for an assumed or *a priori* phase distribution. For the system S containing N_a distinct elements and N_p distinct phases the Gibbs phase rule may be written as

$$F = (N_a - r - 1) - N_p \quad 6)$$

with F denoting the number of degrees of freedom and r denoting the rank of the stoichiometry matrix $A^{\alpha_{aj}}$. The nonnegativity requirement

$$F \geq 0 \quad 7)$$

on the degrees of freedom of the system then upper bounds the maximum number of extant phases at equilibrium according to

$$1 \leq N_p \leq N_a - r - 1, \quad 8)$$

and the system attains a free energy value G^* at equilibrium which is minimal with respect to both the possible phase distributions and the possible molar amounts of the species, the latter subject to the mass constraints in Equation 1. Hence, with P denoting the set of all possible phase distributions, which in view of Equation 8 is finite, and $G^{(p)}$ denoting the Gibbs free energy of S for a particular phase distribution $p \in P$, the mass constrained Gibbs free energy minimization problem takes the mathematical form

$$\text{Fin} \min_{p \in P} \inf \{ G^{(p)}(x_1^1, \dots, x_{N_p}^{N_s}) \mid (x_1^1, \dots, x_{N_p}^{N_s}) \in \mathbb{R}^{N_s N_p}, A^{\alpha_{aj}} x_{j\alpha} = b_a \}. \quad 9)$$

We wish to stress a couple of aspects regarding Equation 9. Firstly, it may be argued from purely physical considerations that there must exist a unique set $x^{*1}_1, \dots, x^{*N_s}_{N_p}$ of molar values of the species that provides the correspondingly unique minimal of equilibrium value G^* of the free energy. At the mathematical level, the set

$$\Omega = \{(x^1_1, \dots, x^{N_s}_{N_p}) \in \mathbb{R}^{N_s N_p} \mid A^{\alpha}_{aj} x_{j\alpha} = b_a, x_{j\alpha} \geq 0, 1 \leq j \leq N_s, 1 \leq \alpha \leq N_p\} \quad (10)$$

is a compact (closed and bounded) convex subset of the $N_p N_s$ -dimensional real number space $\mathbb{R}^{N_s N_p}$. The Gibbs free energy G as approximated in Equations 3-5 is a concave, smooth (i.e., infinitely differentiable) function on the positive hyperoctant of $\mathbb{R}^{N_s N_p}$ and hence in the interior of Ω . A theorem of Kuhn and Tucker (19) then asserts that any local minimizer of Equation 9 is the global minimizer, i.e., that there exists one and only one minimizer for 9. Further, this unique minimizing point is given by (20-22)

$$x^{*j}_{\alpha} = \lim_{\lambda \rightarrow \infty} \frac{\int_{\Omega} x_{j\alpha} e^{-\lambda G}}{\int_{\Omega} e^{-\lambda G}} \quad (11)$$

In physical terms, interpreting λ as time, Equation 11 merely expresses the fact that the equilibrium mole values of the species are given in the asymptotic limit $\lambda \rightarrow \infty$ of their expectation or average values.

The second aspect regarding Equation 9 that needs to be stressed is that of the minimization over the possible phase distributions. The total number of possible phase distributions or equivalently the cardinality $|P|$ of the set P is bounded above by

$$|P| \leq \sum_{N_p=1}^{N_a-r-1} \sum_{\substack{N_{k_1} + \dots + N_{k_t} \leq N_s \\ (N_{k_1}) \dots (N_{k_t})}}^{N_s} \quad (12)$$

The estimate in Equation 12 is conservative and in practice the total number of phase distributions actually realized are considerably lower. Despite this, for a fairly large system ($N_s \geq 50$, $N_a \geq 10$), the phase distribution count grows very rapidly and the problem becomes computationally intractable. Various schemes are being studied and a few important results obtained in this regard. A report on these results will soon be appearing in a forth-coming paper (31). The perhaps most interesting trend that we have observed so far in our numerical studies is that the species appear to behave in the manner of 'bosons' preferring to occupy an already existing phase rather than 'creating' a new one. Our more recent studies are expected to shed further light on this rather intriguing aspect of the problem.

III. PHOEBE

A computer program called PHOEBE for calculating the equilibrium mole values and the Gibbs free energy of a given thermodynamic system has been developed implementing the ideas discussed above. PHOEBE is intended primarily for personal computer use and is fully menu driven. The user generates a specific thermodynamic system from a large database and the equilibrium evolution for the system as a function of temperature can be studied. The average run time for a system comprising approximately 50 species and 10 elements over a range of 10-12 temperatures is about 2 hours. There are no restrictions on the number of species or elements or phases except as dictated by available memory. A mainframe version of PHOEBE is currently under development.

The minimization algorithm adopted is a combination of the "variable metric" algorithms (23) and the projection gradient method (24). Given a point $x^{(0)}$ in the interior of the feasible region Ω , a sequence $\{x^{(n)} | n \in \mathbb{N}\}$ is generated converging to a local (and by convexity, to the global) minimum of G . If $M^{(k)}$ denotes the constraint matrix of the subset of constraints currently active at iteration step k , the idempotent projection matrix P (superscript T denotes matrix transpose),

$$P = I - M^{(k)T} (M^{(k)} M^{(k)T})^{-1} M^{(k)} \quad (13)$$

is constructed to project the gradient of G into the orthogonal complement of the kernel of $M^{(k)}$. It may be observed that the projection matrix P in Equation 13 reduces to the identity matrix when restricted to the kernel of $M^{(k)}$. It should also be observed that if the sequence of points so generated is a sequence of regular points (25) of Ω the first order optimality conditions are satisfied (26). If non-regular or degenerate points are encountered in the generation of the sequence leading to the so-called degeneracy or linear dependency problem, these degenerate points need to be appropriately 'sidestepped' (27),(28). (In any event, a generalized inverse of $M^{(k)} M^{(k)T}$ may be made use of to enter the orthogonal subspace of the kernel of $M^{(k)}$.) The convergence of the sequence is accelerated in its later stages by utilizing the Hessian of G , or if the problem is too large, by approximating the Hessian by a suitable symmetric positive definite matrix. The rate of convergence varies between being linear and superlinear.

In addition to the real Hermiticity of the active or binding constraint matrix $M^{(k)} M^{(k)T}$, its nonnegativity, meaning that each matrix element of $M^{(k)} M^{(k)T}$ is nonnegative, has some important consequences. The eigenvalues of $M^{(k)} M^{(k)T}$ are all real, and in view of the Perron-Frobenius theorems (29-30), the positive eigenvalues are all distinct with the largest positive eigenvalue bounded below by the minimum of the row sums and bounded above by the maximum of the row sums. Also, the existence of a nonnegative eigenvector with eigenvalue equal to the spectral radius of $M^{(k)} M^{(k)T}$ may be asserted. These remarks apply to the Hessian of G as well and are actively utilized in resolving the degeneracy problem if and when it arises.

IV. Conclusions

We have been able to develop a fairly satisfactory algorithm for obtaining numerical solutions to the mass-constrained Gibbs free energy minimization problem. PHOEBE performed quite satisfactorily in test runs on known binary and ternary systems. Some coal systems have also been analyzed and excellent results obtained. However, a few of the coal systems analyzed also produced unrealistic results which led directly to the identification and resolution of the degeneracy problem discussed earlier. Our current attempts are now directed towards representing the free energy of the system more accurately and towards accelerating the convergence of the iterative scheme. We expect to detail these extensions and include comparative studies of program output and experimental data in a forthcoming paper (31).

REFERENCES

- (1) Gibbs, J.W. (1961). *The Scientific Papers of J. Willard Gibbs*, Vol. 1, Dover, New York.
- (2) Bracken, J., and McCormick, G.P. (1968). *Selected Applications of Nonlinear Programming*, Wiley, New York.
- (3) Mylander, W.C., Holmes, R., and McCormick, G.P. (1971). *A guide to SUMT, Version 4*: The computer program implementing the sequential unconstrained minimization technique for nonlinear programming, RAC-P-63, McLean, Virginia.
- (4) Van Zeggeren, F., and Storey, S.H. (1970). *The Computation of Chemical Equilibria*, Cambridge U. Press, New York.
- (5) White, W.B., Johnson, S.M., and Dantzic, G.B. (1958). *J. Chem. Phys.*, **28** (751).
- (6) Oliver, R.C., Stephanou, S.E., and Baier, R.W. (1962). *Chem. Eng.* **69** (121).
- (7) Eriksson, G. (1971). *Acta Chem. Scand.* **25** (2651).
- (8) Eriksson, G. (1974). *Chemica Scripta*, **8** (193).
- (9) Eriksson, G., and Rosen, E. (1973). *Chemica Scripta*, **4** (193).
- (10) Stewart, G., Gruninger, J., Davidovits, P., Yousefian, V., Duff, J., and Weinberg, M. (1981). Computer Modelling of Chemical Processes from Coal Conversion Streams and Related Experiments, DOE/NC/11783-1849, Bedford, Maryland.
- (11) Hastie, J.N., Horton, W.S., Plante, E.R., and Bonnell, D.W. (1982a). Thermodynamic Models of Alkali Vapor Transport in Silicate Systems, High Temp.- High Pressure, **14** (669).
- (12) Hastie, J.N., Horton, W.S., Plante, E.R., and Bonnell, D.W. (1982b). Alkali Vapor Transport in Coal Conversion Systems, ACS Symp. Series, **172** (543).
- (13) Hastie, J.N., and Bonnell, D.W. (1984). A predictive phase equilibrium model for multicomponent oxide mixtures, Part II: Oxides of Na-K-Ca-Mg-Al-Si, *preprint*.

- (14) Friedman, H.L. (1985). *A Course in Statistical Mechanics*, Prentice-Hall, New Jersey.
- (15) McQuarrie, D.A. (1976). *Statistical Mechanics*, Harper and Row, New York.
- (16) Stull, D.R., and Prophet, H. (1971). JANAF Thermochemical Tables, National Bureau of Standards 37, 2nd ed.
- (17) Barin, I., and Knacke, O. (1977). *Thermochemical Properties of Inorganic Substances*, Springer-Verlag, Berlin.
- (18) Robie, R.A., Hemingway, B.S., and Fisher, J.R. (1978). *Thermodynamic Properties of Minerals*, United States Geological Survey Bulletin 1452, U.S. Govt. Printing Office, Washington, D.C.
- (19) Kuhn, H.W., and Tucker, A.W. (1951). Proc. Second Berkeley Symp. on Mathematical Statistics and Probability, U. of California Press, Berkeley.
- (20) Falk, J.E. (1969a). Lagrange multipliers and nonconvex programs, *SIAM J. Control*, 7 (534).
- (21) Falk, J.E. (1969b). Conditions for Global Optimality in Nonlinear Programming, Report No. 69-2, Series in Applied Mathematics, Northwestern U., Evanston, Illinois.
- (22) Pincus, M. (1968). A closed form solution of convex programming problems, Letters to the Editor, *Operat. Res.*, 16 (690).
- (23) Fletcher, R., and Powell, M.J.D. (1963). A rapidly convergent descent method for minimization, *Comput. J.*, 6 (163).
- (24) Rosen, J.B. (1960). The gradient projection method for nonlinear programming, Part I: Linear Constraints, *J. Soc. Ind. Appl. Math* 8 (181).
- (25) Rockafeller, R.T. (1976). Lagrange Multipliers in Optimization, *SIAM-AMS Proc.*, 2 (145).
- (26) Hestenes, M.R. (1966). *Calculus of Variations and Optimal Control Theory*, Wiley, New York.
- (27) Simmons, D.M. (1975). *Nonlinear Programming for Operations Research*, Prentice-Hall, New Jersey.
- (28) McCormick, G.P. (1983). *Nonlinear Programming: Theory, Algorithms, and Applications*, Wiley, New York.
- (29) Horn, R.A., and Johnson, C.A. (1985). *Matrix Analysis*, Cambridge U. Press, New York.
- (30) Lancaster, P., and Tismenetsky, M. (1985). *The Theory of Matrices*, 2nd ed., Academic Press, New York.
- (31) Ramanathan, M., Ness, S., and Kalmanovitch, D.P. (1988). Mass Constrained Gibbs Free Energy Minimization, UNDEMRC preprint.

DEPOSITION OF BEULAH ASH IN A DROP-TUBE FURNACE UNDER SLAGGING CONDITIONS

D.P. Kalmanovitch, C.J. Zygarlicke,
E.N. Steadman and S.A. Benson

Energy & Mineral Research Center
Box 8213, University Station
Grand Forks, ND 58202

INTRODUCTION

The deposition characteristics of coal ash in combustors is a major operational parameter when considering the applicability of a fuel for utilization in a given system. Recent research has shown that drop-tube combustion and deposition experiments can be effectively used to study ash-formation and deposition furnace behavior of coal under carefully controlled conditions (1,2,3). The drop-tube experiment has many advantages over the usual pilot-scale combustion system with respect to deposition studies. A small quantity of coal (400 grams) is needed to perform many tests and the coal feed rate can be carefully controlled. The flow pattern of the fly ash and products of combustion over the ash deposition surface can also be controlled as well as the temperature of the gases and the substrate, gas composition, and residence time. In order to best understand the processes involved in coal ash deposition detailed knowledge of the coal characteristics, combustion conditions, and temperature history of ash particles and deposit surfaces must be obtained. Furthermore, a detailed knowledge of the mineralogy of the various species within the coal allows comparison of the mineralogy of the ashes and deposits formed during combustion. This comparison can give valuable insight into the mechanism of ash formation and the processes involved in the growth and development of strength which lead to the problem of hard-bonded deposits on heat transfer surfaces in the boiler.

The coal chosen for study in this paper is a Beulah, North Dakota lignite. The lignite has been well-studied by a number of researchers and is considered to be somewhat characteristic of the Northern Plains lignite coal. The lignite has high moisture, low ash fusion temperatures, and high alkali - alkaline earth elements present in the ash. A benefit of the coal is the lower sulfur content on a sulfur per million Btu basis compared to eastern coals and high reactivity. The deposition characteristics of the coal are of particular interest as the fuel is known to cause heavy fouling deposits in utility boilers. Indeed, the boilers designed to burn the lignite are about 50% larger than comparable boilers designed to burn high ash-fusion eastern coals. The Beulah lignite is also of importance in ash deposition studies as the coal contains inorganic species both in the mineral phase as well as within the organic matrix of the coal. Extensive research at the University of North Dakota Energy and Minerals Research Center has shown the importance of the organically-bound species on the deposition characteristics in pilot-scale combustion testing (4). Techniques have been developed which can quantify the relative amount of an element which is organically bound or mineral bound. In general, the technique, called chemical fractionation, determines the amount of an inorganic species present in a series of leachates using water, ammonium acetate, and hydrochloric acid (5). The water removes the inorganic species which was loosely associated with the carbonaceous matrix. The ammonium acetate removes a portion of the inorganic constituents, by ion exchange; these constituents are chemically associated with the coal matrix, usually in the form of salts of carboxylic acids. The

hydrochloric acid dissolves the acid-soluble mineral grains such as carbonates, some oxides as well as sulfates and organically coordinated inorganic elements. By comparing the amount of inorganic constituents removed from the coal with the original composition, the amount of inorganics present as insoluble material can be calculated. The insoluble material usually includes inorganic elements associated with acid-insoluble discrete mineral phases such as quartz, pyrite, and clays. In the case of Beulah lignite, chemical fractionation shows that the bulk of the sodium and a large fraction of the calcium is organically bound. These data contrast with eastern coals, where most of the inorganic constituents tend to be associated with the acid-insoluble fraction.

The fate and behavior of the organically bound elements and their reactions with the mineral bound species are of great interest in relation to the deposition characteristics of the coal. Therefore, a detailed understanding of the processes that affect the deposition characteristics of Beulah lignite will give valuable insight into the fundamental aspects of coal ash deposition.

TABLE 1
DROP-TUBE FURNACE RUN CONDITIONS USED TO PRODUCE
INTERMEDIATE ASH FROM BEULAH COAL

Coal Size, μm	53-74
Coal Feed Rate, g/min	0.314
Primary Air, L/min	1.0
Secondary Air, L/min	3.0
Quench Gas, L/min	3.0
Temperature, $^{\circ}\text{C}$	
Secondary Air	930
Furnace Tube skin	1500
Gas Temperature at Inlet to Quench Probe	1450

EXPERIMENTAL PROCEDURE

A sample of Beulah lignite was characterized using chemical fractionation and computer controlled scanning electron microscopy (CCSEM). The latter technique provides the identification and size distribution of the coal minerals. Details of the technique can be found elsewhere (6). Pulverized coal samples were then burned under a range of combustion and deposition conditions in the EMRC drop-tube furnace facility. Details of the drop-tube facility can be found in other publications (1). However, for the purpose of this study, it is important to note that the drop tube furnace has the capability of studying the formation of ash intermediates as

TABLE 2
DROP-TUBE FURNACE RUN CONDITIONS USED TO PRODUCE ASH DEPOSITS
BEULAH DEPOSIT RUN

Feed Rate, g/min	0.272
Coal Size, μm	53-74
Primary Air, L/min	1.0
Secondary Air, L/min	3.0
Quench Air, L/min	8.0
Temperature, $^{\circ}\text{C}$	
Secondary Air	1000
Furnace Tube Skin	1501
Gas Temperature at Constrictor	1478
Substrate	475

• Distance from tip of injector

well as the formation of deposits over a wide range of temperature and residence times. In this study, the determination of intermediate species (entrained ash) and deposits formed under slagging (1450°C) conditions was defined by the gas temperature at the region of the probe and residence time (0.6 to 0.8 sec). The intermediate ash species were cooled with a gas quenching probe and collected using a six-stage multicyclone. Ash deposits were produced by accelerating the fly ash and products of combustion through a ceramic nozzle and impinged on an oxidized boiler steel substrate. In all cases where deposition was studied, the substrate consisted of pre-oxidized carbon steel and was controlled at a given temperature. The conditions used to produce the intermediate ash and deposits are summarized in Table 1 and 2, respectively.

In all cases the intermediate ash from each stage of the multicyclone and deposits were analyzed by x-ray diffraction, scanning electron microscopy and scanning electron microscopy point count (SEMP) techniques. The SEMPC technique was developed at the EMRC to quantify the various phases present in an ash sample. The technique involves the analysis of about 240 points on a polished section of a deposit or a dispersion of ash on cello tape using the electron microprobe facility of the electron microscope with a thin window energy dispersive detector. The compositions of each of the points are transferred to a Lotus[®] spreadsheet which classifies each analyzed point based on chemical composition. The range of classification includes a total of about 30 phases including coal mineral phases, derived mineral phases, crystalline phases, amorphous phases and unclassified phases. Full details of the technique can be found elsewhere (7). Major advantages of the technique include: quantification of the phases, chemical composition of the phases and chemical composition of the point analyzed. The latter is particularly useful for studies where there is insufficient material for bulk chemical analysis. Another important advantage is the ability to determine physical characteristics of each point based

on the chemical composition. For heterogeneous samples such as deposits and fly ash, the chemical composition of the points will be different. However, using the Urbain model of viscosity recently improved by Kalmanovitch and Frank (8), the chemical composition can be used to calculate the viscosity at a given temperature. From these calculations a distribution or population frequency of the viscosity can be determined. This has two advantages. The first is that it describes the heterogeneity of the sample with respect to a key parameter in the deposition process, namely the viscosity of the liquid phase. Second, it allows comparison of the viscosity distribution of specific areas with other areas from the same sample or other samples.

RESULTS AND DISCUSSION

Characterization of Coal

The chemical fractionation results for the coal, Table 3, shows that the bulk of the sodium, magnesium, and calcium are organically bound. The elements removed by HCl include significant amounts of aluminum, calcium, and iron. The extractability with HCl suggests that these elements are associated in the coal as carbonates, acid soluble oxides and organically coordinated elements. The elements remaining after the water, ammonia acetate, and HCl extractions consisted of portions of the aluminum, iron and most of the silicon. The aluminum is likely associated with clay minerals, the silicon with clay minerals and quartz, and the iron is associated as pyrite.

The mineral grains present in the 53-74 μ m sized fractions of coal were sized consistently with the multicyclone particle size controls. The results of the CCSEM mineralogical analysis of the 53-74 μ m sized fraction coal are listed in Table 4. The data shows that the major mineral phase present was aluminosilicate. The aluminosilicate is defined in the technique as mineral grains which contain predominantly Si and Al with no significant presence of another element. Oxygen is not detected by this technique. The aluminosilicate is found to be predominantly in the less than 11 micrometer size range. Only about 30 wt% of the mineral was observed to be larger than 11 microns. There was very little aluminosilicate observed in the size ranges below 2.1 microns. Quartz was also observed in the coal. The bulk of the quartz was in the 4.4-8.0 micron size range. There was very little quartz in the smaller size fractions (less than 2.1 microns) and little quartz above 11 microns. There was very little Fe-aluminosilicate or K-aluminosilicate detected in the coal sample. However, some Ca-aluminosilicate, that is mineral grains containing Si, Al, and Ca, was observed in the sample. The bulk of this phase was present in size ranges less than 4.4 microns. The other mineral phases which were observed in significant quantities were pyrite (Fe and S rich grains), barite (Ba and S rich grains), and gypsum (Ca and S rich grains). The pyrite was present in size ranges below 11.0 microns with the bulk observed in the 8.0-11.0 micron range. The barite was present in the sample both in the large size fractions, above 11.0 microns, and the smaller size fractions, between 1.2 and 8.0 microns. The gypsum was present in significant quantities between 2.1 and 11.0 microns. An important aspect of the mineralogy is that there was no mineral phase observed which contained sodium even though this element is present in the coal ash. Furthermore, the level of calcium present in the various mineral phases does not account for the total amount of calcium present in the coal ash. This data confirms the chemical fractionation data.

TABLE 3
CHEMICAL FRACTIONATION RESULTS FOR BEULAH (6.2% Ash)

	Initial ($\mu\text{g/g}$ mf coal)	Removed by H_2O (%)	Removed by NH_4OAc (%)	Removed by HCl (%)	Remaining (%)
Sodium	5,700	42	57	1	0
Magnesium	2,600	1	97	2	0
Aluminum	3,500	0	0	32	68
Silicon	7,230	1	4	2	93
Potassium	100	65	26	9	0
Calcium	9,700	0	74	26	0
Iron	3,500	0	2	83	15

TABLE 4
BEULAH CCSEM MINERAL COMPOSITION AND DISTRIBUTION
(Results expressed as wt% minerals)

Mineral types	SIZE CATEGORIES (MICRONS)						TOTAL WT. % TOTAL WT. %	
	<1.2	1.2-2.1	2.1-4.4	4.4-8.0	8.0-11.0	>11.0	MINERALS	MINERALS (Coal Basis)
QUARTZ	5.7	7.7	14.5	21.7	29.0	19.1	19.5	1.17
KAOLINITE	41.5	39.5	42.1	53.6	38.1	71.7	51.6	3.11
FE-ALUMINOSILICATE	2.4	1.3	0.3	0.7	0.0	0.0	0.4	0.03
K-ALUMINOSILICATE	0.0	0.0	2.3	0.0	0.0	0.0	0.5	0.03
CA-ALUMINOSILICATE	20.9	24.7	16.4	2.2	0.0	0.0	6.3	0.38
IRON OXIDE	3.6	0.5	0.7	3.9	0.0	0.0	1.6	0.09
PYRITE	4.4	2.1	7.2	1.1	15.3	0.0	4.5	0.26
GYP SUM/BARITE	1.5	5.4	0.4	0.0	0.0	0.0	0.5	0.03
CALCITE	0.0	0.0	0.7	0.0	0.0	0.0	0.1	0.01
BARITE	2.3	7.1	6.1	7.4	0.0	9.2	6.3	0.38
GYP SUM	0.0	0.5	2.8	6.6	12.4	0.0	4.5	0.28
UNKNOWN	17.7	10.5	6.5	2.8	5.2	0.0	4.1	0.24

Characterization of Intermediates

Table 5 lists the results of the SEMPC analysis of the various multicyclone fractions quenched at a gas temperature of 1450°C during the drop-tube combustion of the 53-74 μm Beulah lignite. The first five multicyclones contained various quantities of anorthite, $(\text{CaO} \cdot \text{Al}_2\text{O}_3 \cdot (\text{SiO}_2)_2)$, quartz, melilite (a solid solution series between akermanite, $(\text{CaO})_2 \text{MgO} \cdot (\text{SiO}_2)_2$ and gehlenite, $2\text{CaO} \cdot \text{Al}_2\text{O}_3 \cdot \text{SiO}_2$), and kaolinite derived material. The anorthite and melilite are products of high temperature

recrystallization from a melt phase. The quartz is a residual coal mineral phase. The kaolinite derived material is defined as a point which has a Si/Al molar ratio corresponding to that of kaolinite but has extraneous elements associated with it. The kaolinite derived material and the unclassified material are assumed in our interpretation to be amorphous. In all cases where x-ray diffraction was performed on the same sample as analyzed by SEMPC the latter technique found more crystalline phases than the x-ray diffraction. The points which are overlaps of two adjacent phases may be unclassified. However, these are statistically rare and would not be expected to affect the interpretation of the data as amorphous phases. In general, the SEMPC data shows that the size fractions above 1.2 microns tend to aluminosilicate phases with little sulfate present. The presence of kaolinite derived, anorthite, and melilite phases, shows that there was significant melting and interaction between the Ca, derived from the organic matrix, and the aluminosilicate mineral phase (kaolinite). The relative amounts of quartz in the different size fractions follows the same trend as observed in the CCSEM analysis of the coal. The chemical composition of the material collected in the first five multicyclone filters contained very little sodium. The material in the final filter contained predominantly sodium-calcium sulfate, 76%. The data shows that the sodium and sulfate species tend to be present in, or associated with, the finely dispersed phase, that is, the phase below 1.2 microns.

TABLE 5
SEMPC RESULTS FOR BEULAH MULTICYCLONE SIZE FRACTIONS
(Results expressed as number %)

STAGE #	1	2	3	4	5	6
SIZE, μ m	>11.0	8.0-11.0	4.4-8.0	2.1-4.4	1.2-2.1	<1.2
MASS, %	76.2	4.8	7.5	4.2	3.6	3.7
<hr/>						
Phase						
CaO	3	0	0	0	0	0
Fe-oxides	7.2	2.3	0	0.6	0	0
Kaolinite*	36.2	50.4	63.5	60.2	60.1	10
Anhydrite	0.4	0	0	0	0	5
Anorthite	5.1	3.1	2.9	6.4	1.2	0
Quartz	4.7	2.3	0.7	1.2	0.4	0
Melilite	1.7	2.3	5.8	1.2	1.2	0
Na-Ca-Sulfate	0	0	0	0	0	76
Unclassified	41.7	35.7	34.3	33.9	36.6	8

* kaolinite-derived

Characterization of Deposits

Figure 1 shows the general view of the slag droplet formed on the probe plate. There are two distinct regions, the sintered material near the base and the glassy droplet on the surface of the sintered material. The sintering material at the base of the deposit and slag droplet were each analyzed by the SEMPC technique. Table 6 compares the SEMPC data for the two samples.

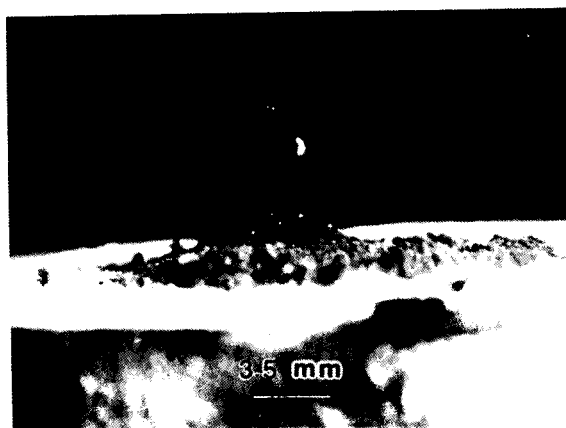


Figure 1. General view of slag formation on the probe plate.

TABLE 6

SEMP-ED DATA FOR SINTERED AND SLAG SAMPLES OF BEULAH ASH (1450°C)

PHASE, percent	SINTERED	SLAG
Calcium oxide	2.0	0.0
Montmorillonite-derived	0.5	1.3
Calcium silicate	1.0	0.0
Iron oxide	10.4	18.9
Kaolinite-derived	12.4	10.6
Anhydrite	1.5	0.4
Anorthite	1.5	1.3
Quartz	7.9	7.5
Melilite	0.5	0.0
Dicalcium silicate	0.5	0.0
Calcium derived	6.0	0.9
Unclassified	56.1	58.6

The results of the SEMPC analysis indicates that there are different phases present in the base of the deposit than in the slag at the top of the deposit. The SEMPC analysis of the base of the deposit corresponds very well with the analysis of the first stage of the multicyclone. All the phases observed in the first multicyclone stage were observed in the base of the deposit and the relative proportion of the phases are very similar. However, there was more calcium derived and less kaolinite derived material in the deposit base than was observed in the multicyclone. This is presumably due to the effect of residence time, milliseconds for the multicyclone sample compared to minutes for the deposit.

The slag deposit had similar phases to the base deposits. However, there were some significant differences. There was only one calcium aluminosilicate phase, that of anorthite, observed in the slag samples. This contrasts with the base where calcium silicate, dicalcium silicate, and melilite were observed in the base as well as the multicyclone samples. No calcium oxide was observed and the level of calcium-derived material was much lower in the slag as compared to the deposit base. The data indicates that the sample was approaching thermal equilibrium due to the long residence time and the higher temperature, approaching 1450°C. The composition of the material excluding quartz and iron oxide phases, would give a predominantly calcium aluminum silicate system. The normalized CaO-FeO-Al₂O₃-SiO₂ composition when plotted on the equilibrium phase diagram show that the composition lies in the primary phase of anorthite with a liquidus temperature of about 1400°C.

The SEMPC also gives data on the chemical composition of the sample studied. Table 7 compares the chemical composition of the sample base and slag deposit. Also included in Table 7 is the Si/Al molar ratio and the chemical composition of the unclassified points and the silicate phases observed in the two samples. The latter data is obtained by deleting the compositions of the quartz, iron oxide, calcium derived and anhydrite points from the data base and recalculating the average chemical composition.

The composition of the base was very different than the slag. Most notable differences were with the levels of SiO₂, Al₂O₃, CaO, and SO₃. The base had less SiO₂ and Al₂O₃ and greater CaO and SO₃ than the slag. This confirms the earlier observation that the initial deposit adhesion and growth is via a sulfate mechanism whereas the slag is via a silicate based matrix (9,10). The Si/Al molar ratio for the base and slag are relatively similar. This indicates that there is little change in the transport of silicate and aluminosilicate species to both types of deposit. The higher levels of CaO and SO₃ in the base of the deposit would suggest that there is a preferential deposition of the calcium-rich species on deposit surfaces still cooled by the probe. The level of SO₃ tends to indicate that the sulfation of the calcium occurred after the deposition of the calcium rich grains.

The CCSEM data on the coal and the chemical fractionation data indicated that there was relatively limited mineral bound calcium in the coal, the bulk was organically bound. This would tend to indicate that the transport of calcium would be as finely dispersed calcium oxide/calcium sulfate particles. However, the SEMPC data on the multicyclone samples indicate that significant calcium was associated with the large size fractions which were also rich in aluminum and silicon. It was also noted that the SEMPC data for the first multicyclone was very similar to the SEMPC data for the base of the deposit. This indicates that the major mass transport to the deposition probe is via the large size fractions. The presence of such a high level of calcium

TABLE 7
CHEMICAL COMPOSITION OF DEPOSITS (SEMPG)

<u>Wt. %</u>	<u>Base</u>	<u>Slag</u>
SiO ₂	25.5	39.8
Al ₂ O ₃	10.0	16.5
Fe ₂ O ₃	21.0	30.7
TiO ₂	0.7	0.4
P ₂ O ₅	0.0	0.0
CaO	31.3	9.8
MgO	2.0	0.3
Na ₂ O	0.2	0.8
K ₂ O	0.1	0.3
SO ₃	8.8	1.3
Si/Al molar ratio	2.05	2.17

CHEMICAL COMPOSITION OF UNCLASSIFIED AND SILICATE PHASES

<u>Wt. %</u>	<u>Base</u>	<u>Slag</u>
SiO ₂	24.9	50.6
Al ₂ O ₃	13.5	24.9
Fe ₂ O ₃	10.7	11.3
TiO ₂	1.0	0.6
P ₂ O ₅	0.0	0.0
CaO	37.6	13.1
MgO	2.6	0.4
Na ₂ O	0.1	1.1
K ₂ O	0.2	0.4
SO ₃	9.1	1.3

associated with the aluminosilicate species indicates that melting and assimilation occurred at the relatively high temperatures. The entrained ash would not be expected to see a temperature below the gas temperature of 1450°C. These high temperatures and relatively short residence times preclude the formation of sulfate species. However, calcium aluminosilicate phases, both liquid and crystalline, are stable at these temperatures. The reaction of calcium with the aluminosilicate

phases is evidenced by the presence of phases such as melilite, anorthite, calcium silicate, and dicalcium silicate in the multicyclone fractions. These phases are not the product of thermal decomposition of mineral phases but are products of recrystallization from a calcium rich melt phase.

The level of calcium in the multicyclone fractions precludes total reaction with the aluminosilicate phases, and once deposited, the calcium rich material will tend to react with sulfate at lower temperatures. This leads to the low level of calcium in the slag deposit. This process can be understood if one considers that the material which will form a melt phase at these temperatures will be the elements intimately associated with the aluminosilicate phases. Refractory oxides such as calcium oxide which have not reacted to any extent with the aluminosilicate will not be associated with the phase forming the liquid drop and will tend to be expelled from the surface of the droplet and removed by the scrubbing action of the gas stream. Substantiation of this process can be seen with the analysis of the relative levels of sodium in the two samples. The sodium was observed to be present predominantly in the final filter of the multicyclone along with calcium sulfate. The stability of sodium sulfate is less than that of calcium sulfate at 1450°C. Therefore, the low level of sodium in the base deposit is due to the fact that it was not transported along with the aluminosilicate phases. The relative enrichment in the slag is due to thermal dissociation of the sulfate species and reaction with the aluminosilicate phase. Sodium has a greater affinity for aluminosilicate melt phase than calcium at 1450°C. A large proportion of the sodium is present in the very small size fractions. Under the conditions used the bulk of the sodium must have been carried past the deposit probe along with the gaseous products of combustion. This shows why sodium is such a problem in the cooler regions of the boiler, i.e. the convective pass where conditions tend to increase the stability of sodium sulfate and other alkali-rich species.

CONCLUSIONS

The detailed analysis of a Beulah lignite sample and the deposits formed from the fuel in a drop tube furnace at a gas temperature of 1450°C has given valuable insight in the mechanisms of mass transport and deposit initiation and growth. The coal was shown by chemical fractionation and computer controlled scanning electron microscopy (CCSEM) to contain aluminosilicate species and organically bound calcium and sodium. The entrained ash, as sampled using a multicyclone, was shown, by using a novel technique called scanning electron microscopy point count (SEMP), to contain high temperature calcium silicate and calcium aluminosilicate phases in the size fractions above 1.2 microns and calcium and sodium-calcium sulfate in the less than 1.2 micron range. The deposit formed from the coal ash with a probe surface temperature of 350°C and gas temperature of 1450°C was comprised of a small sintered base with a molten slag droplet on the surface; both sections were characterized using SEMPC. This technique showed that the deposit base had a similar chemical composition and phase assemblage as the largest multicyclone fraction, i.e. above 11.0 microns. The slag deposit however, had lower CaO and SO₃ than the base of the deposit and the calcium aluminosilicate phase observed was consistent with that expected for the melt phase from thermal equilibrium phase diagrams. Further analysis of the SEMPC data showed that the bulk of the material was transported to the probe surface with the aluminosilicate fraction. The different levels of CaO in the two sections of the deposit were consistent with the observed association of calcium with the aluminosilicate phases in the multicyclone samples and the known relative thermal stability of calcium aluminosilicates over calcium sulfate at 1450°C. The level of sodium was low in both samples of the deposit, and low in all multicyclone

samples except the final filter material. The low level of sodium in the deposit is consistent with the sodium being present in a finely dispersed form which was carried past the deposit with the combustion gases.

The study has shown the importance of detailed analysis of the coal, intermediates, and deposits in understanding the mechanisms and processes which affect deposit formation and growth in a drop-tube furnace. The results of this study can be summarized as follows:

- o Organically bound calcium will react with clay species to form calcium-rich aluminosilicates at short residence times.
- o The bulk of the calcium is transported via these calcium-rich aluminosilicates.
- o Sodium (organically bound) as sodium calcium sulfate was formed in the smallest size fractions.
- o The mass transport to the cooled metal surface tends to be that of the largest size fraction of the multicyclone (above 11 microns).
- o Sulfation of the calcium tends to occur after deposition and only in the cooler regions of the deposit (nearest the metal surface).
- o The matrix in the slag section of the deposit is predominantly calcium aluminosilicate and tends to approach thermal equilibrium.
- o The similarity in Si/Al molar ratio in the base and slag sections of the deposit indicates similar transport mechanisms throughout the deposit growth cycle.
- o Relatively low concentrations of Ca in the slag was indicated to be due to the poor assimilation of refractory calcium oxide rich regions into the melt phase.
- o Sodium enrichment in the slag relative to the base was consistent with the great affinity of sodium in silicate melts.
- o The low level of sodium in the deposit indicates that the sodium was entrained in the gas phase and passed over the probe and deposit under then slagging conditions.

ACKNOWLEDGMENTS

The collection and characterization of the intermediate ash material was performed under contract with the U.S. Department of Energy Pittsburgh Energy Technology Center. Philip Goldberg is the project manager. Formation and characterization of ash deposits was performed under contract with the Advanced Combustion Engineering Research Center, Brigham Young University. L. Douglas Smoot is the Project Manager. The authors would like to thank Mr. Goldberg and Dr. Smoot for their support of this work.

REFERENCES

1. Benson, S.A., E.N. Steadman, and D.P. Kalmanovitch, "Studies of the Formation of Alkali and Alkaline Earth Aluminosilicates During Combustion Using a Laboratory Scale Furnace," Presented at the EPRI Conference on Effects of Coal Quality on Power Plants, Atlanta, October 13-15, 1987.
2. Benson, S.A. and Austin, L.G., "Laboratory Ash Deposition Studies of a Gravity-fractionated Coal," 88-JPGC/Pwr-4.
3. Benson, S.A., W.H. Puffe, M.L. Jones, R.W. Borio, J.F. Durant, and A.K. Mehta, "Laboratory-scale Ash Deposition Studies of a Size and Gravity Fractionated Coal", Proceedings of the American Flame Research Committee 1988 Fall International Symposium, October 4-6, 1988.
4. Sondreal, E.A., Tufte, P.H., and Beckering, W. "Ash Fouling in the Combustion of Low Rank Western U.S. Coals", Combustion Science and Technology, Vol. 16, 95-110, 1977.
5. Benson, S.A. and P.L. Holm, "Comparison of Inorganic Constituents in Three Low-Rank Coals," Ind. Eng. Chem, Prod. Res. Dev., 24, 145-149, 1985.
6. Huggins, F.E., and D.A. Kosmack, 1980, Coal Mineralogies by SEM automatic image analysis: Scanning Electron Microscopy, 1980, I, AMF O'Hare (Chicago), IL 60666, p. 531-540.
7. Kalmanovitch, D.P., G.G. Montgomery and E.N. Steadman, ASME Paper Number 87-JPGC-FACT-4, 1987.
8. Kalmanovitch, D.P. and M. Frank, "An Effective Model of Viscosity for Ash Deposition Phenomena", presented at the conference on Mineral Matter and Ash Deposition from Coal, The Engineering Foundation, Santa Barbara, CA, February 21-26, 1988.
9. Benson, S.A. and L.G. Austin, "Study of Slag Deposit Initiation Using a Laboratory-Scale Furnace", Presented at the Conference on Mineral Matter and Ash Deposition from Coal, The Engineering Foundation, Santa Barbara, CA, February 21-26, 1988.
10. Jones, M.L. and S.A. Benson, "An Overview of Fouling and Slagging from Western Coals", Presented at the EPRI Conference on Effects of Coal Quality on Power Plants", Atlanta, GA, October 13-15, 1987.

A CLASSIFICATION OF COAL-FIRED BOILER DEPOSITS

Roderick M. Hatt
Island Creek Corporation
Lexington, KY 40579

Susan M. Rimmer
Department of Geological Sciences
University of Kentucky
Lexington, KY 40506

INTRODUCTION

Ash deposition in boilers has been studied by numerous investigators from virtually all areas of physical science. Several books (1) (2), and publications too numerous to reference have been published on this subject. Unfortunately the information flow between boiler operators and researchers has not always been ideal. In the absence of a workable classification system, valuable information concerning the nature and conditions of formation of boiler deposits may be lost. Field observations can greatly enhance information derived from laboratory study, and can lead to a more meaningful interpretation of the causes and, ultimately, to the solution of boiler deposits. As such, the system proposed here provides basic steps in the documentation of field observations together with a simple megascopic and microscopical classification scheme.

Whereas this system was designed to describe deposits from coal-fired steam generators, it may be applied to other environments or equipment with similar high-temperature mineral transformations. This system only addresses cooled deposits, as opposed to those that exist at the higher temperatures of boiler operation.

DEPOSITS IN BOILERS: FIELD OBSERVATIONS

Boiler Description

The type of boiler influences the properties and significance of the deposits (3). A simple description of the boiler and operating conditions provides information on processes and environments to which the coal and ash may have been exposed. This description should include, at a minimum, firing method (stoker, PC, cyclone), unit size including steam flow, heat input and plan area, and, if known, gas temperatures and velocities throughout the system. All of these variables can influence deposit formation (4). Much of this information, in addition to the proximate, ultimate and heating values for the design fuel, is provided on the boiler manufacturers' performance sheet.

Fuel Description

Variations in ash content and composition of the feed coal can lead to a variety of boiler problems as discussed by Hatt (5). A

detailed description of the feed coal is important and could include, where available, proximate, HHV, total sulfur, sulfur forms, ash-fusion temperatures, and ash chemistry. Other, more detailed coal analyses can be helpful in determining coal quality impacts on deposit formation (6).

Location of Deposits

The physical appearance of the deposit should be given using the megascopic system presented below, together with location and extent of the deposit, preferably by providing a simple sketch of the boiler in a side and top sectional view (as shown in Figure 1). Photographic documentation is useful but can be difficult to obtain. The location of deposit samples taken during the boiler inspection can be documented on this sketch. Samples should be taken to represent the entire deposit. Guidelines on sampling can be found in the British Standard (7), and in a future publication (8).

MEGASCOPIC CLASSIFICATION

Boiler deposits can be classified as either molten deposits (slags) or deposits bonded by sulfate salts (fouling deposits) (3). Each type of deposit has characteristics that can be used to describe the material and can provide clues about the conditions of formation. Figure 2 shows an outline of the megascopic system.

Slags or Molten Deposits

Slags or molten deposits can be classified into four basic types.

- Metallic - These slags have a metallic luster and are usually associated with the combustion of pyrite-rich coals under reducing conditions. The high specific gravity of the metal generally allows it to separate from the slag, and to remain isolated from any subsequent oxidizing atmospheres (Figure 3a).
- Amorphous - Amorphous slags are dark, solid, glassy, and generally show a conchoidal fracture. Amorphous slags are usually found in the higher temperature regions of the boiler (Figure 3b).
- Vesicular - Glassy slags with trapped bubbles (a sponge-like appearance) can be classified as vesicular. These are usually associated with higher temperature regions in the boilers. Trapped gas bubbles may be distorted due to viscous flow (Figure 3c).
- Sintered - Deposits that are composed of partially fused particles may be classified as sintered. These are gritty in texture, are typically found in

the upper furnace and convection passes, and may be associated with vesicular slags (Figure 3d).

Additional useful information could include physical characteristics such as tube imprints, gas flow direction, color, and size.

Fouling Deposits

Fouling deposits are differentiated from slags according to the type of bonding that occurs between particles. In slags, bonding is produced by melting or fusion of the ash particles; in fouling deposits, the ash particles are bound together by sulfate salts (3). Gas temperatures in furnace regions where fouling occurs are generally lower than those associated with slagging; there is, however, some overlap where both bonding mechanisms can occur. Fouling deposits are generally dull in luster, have a gritty or brick-like texture, and lack the glassy and vesicular textures observed in slags. Distinguishing features include color, shape, size, internal structures such as laminations, and strength. The location and orientation of the deposit with respect to the tubes and gas flow can provide additional information. Strength is one of the most important characteristics of fouling deposits, and may be categorized using the following relative index:

- Very Strong - Deposits are hard, and may be broken only with the aid of a hammer, chisel or other tool.
- Strong - Deposits can be broken by hand but do not crumble easily.
- Weak - Deposits crumble when handled.
- Unconsolidated - Deposits are not bonded and result from accumulations of material which settle out of the flue gas.

Although qualitative in nature, this strength rating provides an indication of the degree of bonding in the deposit, and can be used to determine the level of difficulty that removal of a deposit could present.

MICROSCOPIC CLASSIFICATION

Microscopic examination of ash deposits indicates the degree and nature of bonding. This microscopic classification system is designed to be used with both polarized-light and scanning electron microscopy. It is analogous to the megascopic system in that it differentiates between slagging and fouling deposits based on the presence or absence of sulfate salts. In many cases several phases may be discernible under the microscope, i.e. both amorphous and vesicular, or sintered with sulfate salts. This can make the categorization of some deposits problematic, and in these cases all of the appropriate descriptions should be noted. Figure 4 is an outline of the microscopic system.

Amorphous Slag Phases

Amorphous slags are usually alumino-silicate melts with varying amounts of basic (fluxing) elements. Using a polarizing microscope, crushed samples can be used to show the conchoidal fracture. Magnetic minerals can be identified by placing a magnet near the glass slide on which the crushed sample is mounted in oil or water. In thin section, amorphous slags do not exhibit any birefringence. Conchoidal fracture can also be observed using a scanning electron microscope. Quartz can be trapped inside of the slag as an inclusion; dendritic species can be formed during cooling of the deposit during unit shut down. Mullite needles are also present in some samples. (3) The presence of bubbles and their shape provides information on the viscosity and gas flow direction. Figures 5a & 5b shows several examples of amorphous slags viewed microscopically.

Partially Fused or Sintered Phases

Sintered phases are characterized by the presence of fused ash particles. The degree of fusion can vary within a single sample, and can tend towards complete fusion of the particles, i.e., the formation of an amorphous slag. The degree of fusion between particles has been correlated with the strength of the deposits (2) and with the chemical composition (7).

In the classification system presented here the degree of fusion between particles is not quantified; only the presence or absence of fusion is noted. If the ash exhibits no fusion or bonding, other classification systems, such as that proposed for fly ash by Fisher (8) or Roy (9) can be used. In addition, sintered deposits may contain non-bonded or slightly bonded particles, which add considerable bulk to the deposit. Figures 5c & 5d show examples of sintered ash particles.

Sulfate Salt Bonding

The presence of sulfate salt or similar bonding material is indicative of fouling mechanisms. The classification of these deposits is similar to that of slag, i.e. totally bonded versus partially bonded.

Total Bonding

When the individual fly-ash particles are bonded totally by sulfate salt, the deposit is generally hard and is representative of the classic fouling deposit. Another category of a totally bonded deposit occurs where sintered deposits are enveloped in a sulfate "glue." The combination of both sintered and fouling bond types makes these deposits particularly hard to remove. These dual-bonded deposits represent slagging and fouling at the same location, and possibly at the same time. Sulfate-salt bonding is not generally associated with amorphous slags. (Figure 6a & b)

Partial Bonding and Surface Crystals

Partial sulfate salt bonding and surface crystals can be observed in some deposits, with the degree of bonding increasing towards totally bonded types of deposits. The presence of this partial bonding can add strength to a sintered type slag. (Figures 6c & 6d)

CONCLUSIONS

The classification system presented here represents an initial attempt in the description of boiler deposits. The use of such a system should aid in communication about the nature of deposits encountered, allowing the engineer or operator to more precisely communicate his problem with the researcher.

REFERENCES

1. Vorres, K.S., Editor, "Mineral Matter and Ash in Coal," ACS Symposium Series 301. American Chemical Society, 1986.
2. Raask, E., "Mineral Impurities in Coal Combustion," Hemisphere Publishing Corp., New York, N.Y. 1985.
3. The Babcock and Wilcox Company, "Steam, Its Generation and Use," 38th Edition, 1975.
4. Hsu, L.L.; Kubarych, K.G.; Stetson, A.R.; and Metcalfe, A.G., "Mechanisms of Fouling, Slagging and Corrosion by Pulverized Coal Combustion," Final Report US DOE Contract No. DE-AC22-81PC40272, June, 1984.
5. Hatt, R.M., "Prediction and Evaluation of Coal Performance Based on Laboratory Analyses," from Proceedings of the 5th International Coal Testing Conf., February 11-13, 1986, Lexington, KY pp 79-87.
6. Borio, R.W. and Narciso, Jr., R.R., "The Use of Gravity Fractionation Techniques for Assessing Slagging and Fouling Potential of Coal Ash." Winter Annual Meeting of ASTM, December, 1978.
7. British Standard - BS2455: Methods of Sampling and Examining Deposits from Boilers and Associated Industrial Plant, Part 2, 1983.
8. Hatt, R.M., "Boiler Deposit Sampling Guidelines." To be published; available on request.
9. Hatt, R.M. and Bull, D.L., "Morphological and Chemical Relationships of Deposits Formed in a Full-Scale Steam Generator," Engineering Foundation Conference on Mineral Matter and Ash Deposition from Coal Santa Barbara, CA February 21-26, 1988.

10. Fisher, G.L., et al., "Physical and Morphological Studies of Size Classified Coal Fly Ash," Environmental Science and Technology V. 12 no. 4 p447-451, 178.
11. Roy, W.R., et al., Coal Fly Ash: A Review of the Literature and Proposed Classification System with Emphasis on Environmental Impacts, Illinois State Geological Survey, Environmental Geology notes 96, April, 1981.

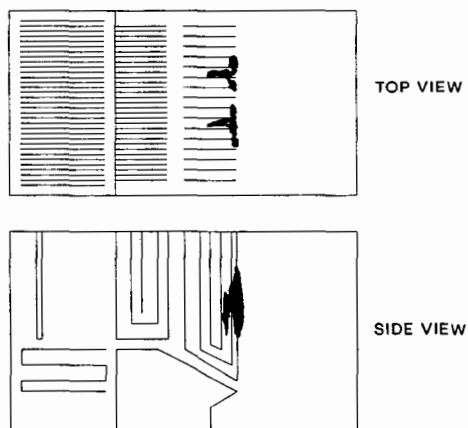


FIGURE 1. SIMPLE SKETCH OF BOILER

DEPOSIT	SLAG (FUSED DEPOSITS)	METALLIC	COMMONLY DERIVED FROM PYRITE DURING COMBUSTION UNDER REDUCING CONDITIONS
		AMORPHOUS	TYPICALLY FOUND IN HIGH- TEMP. ZONES OF BOILERS AND WITH LOW FUSION COAL
		VESICULAR	AMORPHOUS SLAG WITH BUBBLES
		SINTERED	PARTIALLY FUSED PARTICLES COMMONLY FOUND IN CONVECTION PASSES OF BOILERS
	FOULING (SULFATE SALTS)	VERY STRONG	CANNOT BE BROKEN WITH HANDS, YOU MUST USE A TOOL
		STRONG	CAN BE BROKEN WITH HANDS, BUT DOES NOT CRUMBLE
		WEAK	DEPOSITS CRUMBLE WHEN HANDLED
		UNCONSOLIDATED	DUST ACCUMULATIONS

FIGURE 2. MEGASCOPIC CLASSIFICATION SYSTEM

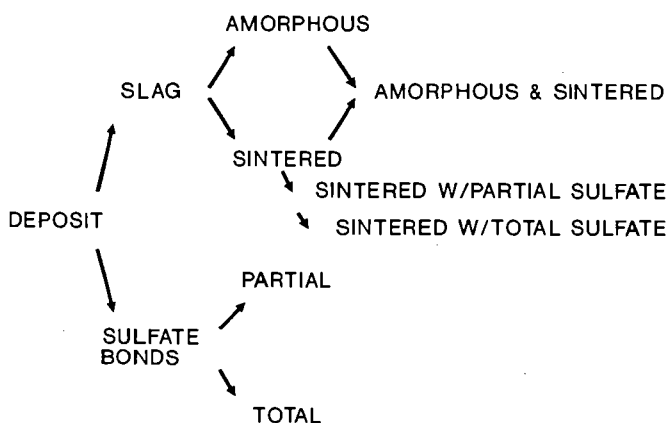
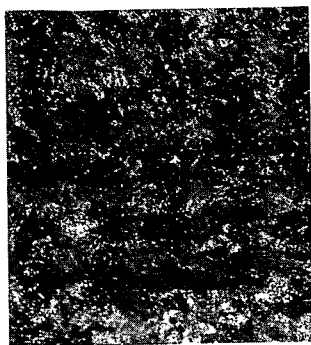


FIGURE 4. OUTLINE OF MICROSCOPIC SYSTEM



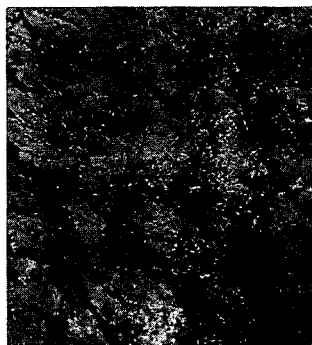
a



b



c



d

Figure 3, Examples of different types of slags: a, Metallic; b, Amorphous; c, Vesicular; d, Sintered.



a



b



c

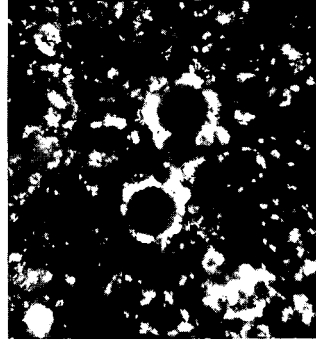


d

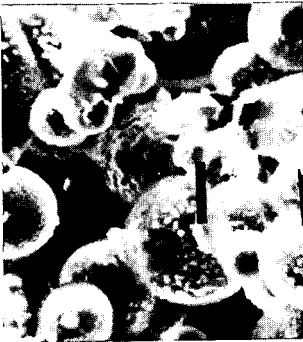
Figure 5. Microscopic view of slags: a, Dendritic crystals in amorphous slag (plain polarized light, thin section); b, Mullite crystals in vesicular slag (plain polarized light, thin section); c, Sintered slag with quartz crystal (PPL, thin section); d, Sintered slag (SEM, plain mount).



a



b



c



d

Figure 6. Microscopic view of Fouling Deposits: a, Total sulfate bonding (plain polarized light, crushed sample in oil); b, Total sulfate bonding (cross polars, thin section); c, Partial sulfate bonding of sintered deposit (SEM, plain mount); d, Surface crystals on sintered deposit (SEM, plain mount).

CALCULATIONS OF THE INFLUENCE OF ADDITIVES ON COAL COMBUSTION DEPOSITS

M. Blander, S. Sinha
Argonne National Laboratory
Argonne, Illinois 60439-4837

A. Pelton, G. Eriksson
Ecole Polytechnique de Montréal
Montréal, Québec, Canada H3C 3A7

INTRODUCTION

The complex chemistry of coal combustion involves hundreds of species in gaseous, solid, and liquid phases, with some of these being solution phases. We have developed new robust calculational techniques capable of defining the total chemistry of coal combustion and of the complex solid and liquid silicate and sulfate solutions involved.^{1,2} The results indicate that coal combustion chemistry is more complex than had been believed and that kinetic factors can enhance fouling and corrosion by liquid condensates. In this paper, we examine the changes in chemistry due to additions of CaCO_3 (to desulfurize the gaseous effluents) and of NaCl and CaCl_2 (which are recommended as deicers or to increase the conductivity of effluents in electrostatic precipitators).³ The results reveal the chemical changes due to these additives; these should be important in defining a strategy for making such additions. In addition, we also impose an expected kinetic constraint on the chemical reactions. Such constraints should, ultimately, prove to be very important in real systems. Ultimately, in order to take these into account in deducing the total chemistry of combustion, a coupled calculational-experimental study of combustion should be carried out to define the important kinetic factors.

CALCULATIONAL METHODS

A robust updated version of SOLGASMIX⁴ was used to perform these calculations using data on the large number of possible species in the F*A*C*T⁵ data base. In addition to the gaseous, solid, and liquid species in the data base, we incorporated a method for calculating the thermodynamic properties of liquid silicates^{6,7,8} and a method for calculations of the properties of sulfates using the data deduced in our analysis of the Na_2SO_4 - CaSO_4 - MgSO_4 ternary molten salt system and of the CaSO_4 - MgSO_4 and Na_2SO_4 - CaSO_4 - MgSO_4 solid solutions that crystallize from the sulfate melts. This analysis led to an assessed phase diagram for the ternary sulfate, which was necessary in order to define the chemical properties and the range of stability of the corrosive liquid sulfate phase that forms from the coal combustion condensates.

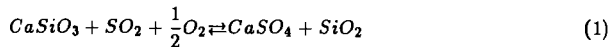
COMBUSTION OF ILLINOIS #6 COAL

We have previously examined the equilibrium combustion products of Illinois #6 coal and have imposed an expected kinetic constraint on the formation of $\text{NaAlSi}_3\text{O}_8$ and NaAlSiO_4 to illustrate the importance of kinetic factors.^{1,2} In this paper, we compare these constrained equilibrium calculations with calculations performed with the addition of CaCO_3 , NaCl , or CaCl_2 . These additions lead to changes in the total chemistry, and our results can be used to deduce strategies for making such additions. The overall composition of Illinois #6 coal is

given in Table I. In the calculations that follow, we combusted 100 grams of coal with an excess of oxygen (237 grams O_2 added as air). To this mixture, we added 6.25 grams of $CaCO_3$, or 0.4 grams of $NaCl$, or 0.4 grams of $CaCl_2$. The additives lead to complex changes in the total chemistry.

In Tables II, III, and IV, we present a selection of the results of our calculations of condensates with and without $CaCO_3$ addition that illustrate the important changes in chemistry brought about by the additive. In Table II, we give calculations for the composition of liquid silicates at temperatures where they are present. With no added $CaCO_3$, a molten silica-rich silicate exists down to about 1260 K, where a small amount of sulfate forms. With the addition of $CaCO_3$, the amount of molten silicate is increased significantly at the higher temperatures, mostly because of an increase in the CaO content. As a consequence, the liquid is not as silica rich and will be considerably less viscous than when no limestone is added. Because the activity coefficients of all the basic components of the slag are generally higher at low silica than at high silica contents, and also because of the high CaO concentration, this slag reacts more readily with $SO_2 + \frac{1}{2}O_2$ (and SO_3) in the gas phase than does a high silica slag and forms a liquid sulfate phase between 1350 and 1400 K with $CaCO_3$ additions. This temperature is considerably higher than the temperature of first formation of liquid sulfate with no $CaCO_3$ addition, because the activities of the basic oxides (CaO , MgO , and Na_2O) in the silica saturated acid slag are significantly lower than in the less acid slags found with limestone addition and because the tendency to form sulfate increases with a decrease in temperature, i.e., the standard entropy of reaction of the oxides with gaseous SO_2 and O_2 is negative.

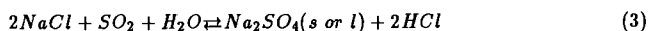
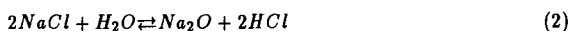
For the case with $CaCO_3$ addition, the decrease in the amount of slag at 1350 K (to 0.15 g) is accompanied by the appearance of a significant amount of sulfate, largely Na_2SO_4 , as exhibited in Table III. These relative amounts remain essentially the same, at least down to 1300 K (Table III). The slag disappears by 1250 K (Table II) and somewhat more sulfate appears (Table III) at the expense of the slag constituents and $CaSiO_3$ (Table IV). The SO_3 ($SO_2 + \frac{1}{2}O_2$) in the gas phase is a stronger "acid" at these temperatures than even SiO_2 . Thus, one of the reactions that has taken place to a small extent between 1250 K and 1300 K is



with the product SiO_2 appearing as a new phase (Table IV). At yet lower temperatures, the liquid sulfate crystallizes to form two solid solutions and there is an increasing tendency for reactions of the remaining alkaline earth silicates or aluminosilicates with $SO_2 + \frac{1}{2}O_2$ to form sulfates. Consequently, upon cooling, solid $CaSiO_3$ (wollastonite) disappears before 1150 K, and $CaAl_2Si_2O_8$ (anorthite) and $CaMg(SiO_3)_2$ (diopside) disappear before 1050 K, with a consequent increase in the amount of sulfate solid solutions and silica at both temperatures. Essentially, all of the alkali and alkaline earth oxides are thus converted to sulfate before 1050 K. This result holds with or without limestone additions because of the excess of oxides of sulfur in the gas. The total amount of sulfate is, of course, much larger with limestone additions because of an increased amount of $CaSO_4$ with a consequent decrease (relative to no limestone addition) in sulfur oxides of 68% at 1050 K and 1000 K. In real systems, kinetic factors could lead to desulfurization percentages less than this. The kinetics of reactions to form sulfates from solids such as $CaAl_2Si_2O_8$, $CaSiO_3$, or $CaMg(SiO_3)_2$ could be too slow to go to completion. If field data indicate this to be true, then our calculations can be used to define a strategy for improved

desulfurization. In addition, because a significant amount of SO_2 remains in the gas, greater desulfurization is possible in principle with larger additions of CaCO_3 .

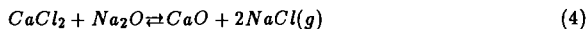
The addition of 0.4 grams of NaCl does not lead to large differences in the chemistry. NaCl is largely present in the vapor at high temperatures, which reacts at lower temperatures to form either the oxide or sulfate and HCl by the reactions



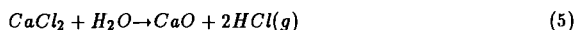
where the oxide in (2) could enter the slag or form a solid silicate. More HCl than NaCl is present in the vapor at 1300 K or lower with a liquid sulfate appearing between 1250 K and 1300 K.

For very large additions of NaCl (3.5 grams) to 100 grams of coal, the amount of Na_2O in the slag increases noticeably. However, most of the NaCl is in the vapor phase at the higher temperatures. In this case, the amount of HCl exceeds that of NaCl at 1250 K, at which temperature a liquid sulfate is also present. (There is no sulfate phase at 1300 K.)

With the addition of 0.4 grams of CaCl_2 , there is a significant decrease in the amount of slag (e.g., 0.49 grams at 1300 K), largely due to the formation of solid $\text{CaAl}_2\text{Si}_2\text{O}_8$ (anorthite) by the reactions



at high temperatures and



at low temperatures, where the CaO produced reacts with slag and aluminosilicates to form solid anorthite.

With no constraint on the formation of $\text{NaAlSi}_3\text{O}_8$ (albite), there is a similar effect on the amount of slag produced with NaCl additions. Removal of this constraint on albite formation with NaCl additions would be justified because albite forms at considerably higher temperatures with NaCl additions than without these additions, and the causes of the kinetic constraint would not hold at such temperatures. However, in order to explore this class of reactions more completely, we will have to perform analyses of alumina containing slag systems that are consistent with the liquidus temperatures of anorthite and albite and incorporate these analyses into our calculations. The possibility of reducing the amount of slag and the temperature range of liquid slag stability by suitable additives is important enough to expend an effort on the above analyses. Irrespective of the results of the above analyses, the volatility of sodium chloride and the increasing tendency of chlorides to form sulfates and HCl as temperature decreases partially controls the changes in the final products of combustion with chloride additives.

DISCUSSION

Our calculations provide information that could be useful for defining strategies for the use of additives. Two results of our calculations for limestone addition are clearly significant for desulfurization strategy. First, more slag is produced and it is considerably less viscous than those produced with no additives. Secondly, the CaO from the limestone forms silicates at high temperatures that react with sulfur oxides at lower temperatures to form sulfates. There is a good likelihood that this sulfate-forming reaction will not go to completion because of kinetic

barriers to reactions involving complex silicates. Consequently, addition of limestone at lower temperatures would avoid the complexity and kinetic problems involved in additions to the coal and if the additives can desulfurize effectively at temperatures of about 1200 K or below, the amount and temperature range of stability of the corrosive liquid sulfate would be minimized.

Additions of chlorides as deicers tend to produce gaseous HCl at low temperatures, and boiler designs and materials of construction should be chosen to minimize corrosion by this species. With large chloride additions, the stability and amount of molten slag produced will be very different from the case with no additions. Precise results require development of means to represent the slag chemistry with alumina as a constituent. Our calculations suggest that large additions of CaCl_2 and NaCl might decrease the amount and temperature range of stability of a liquid slag.

Further work is necessary to extend our slag model to incorporate alumina as a component to better define the total chemistry, especially for the case with chloride additions. In addition, a coupled experimental-calculational research program would help to define important kinetic factors to incorporate into our calculations as constraints and could ultimately permit us to define the total combustion chemistry of coal.

ACKNOWLEDGMENT

This work was supported by the U.S. Department of Energy, Office of Basic Energy Sciences, Division of Materials Sciences, under Contract No. W-31-109-ENG-38.

REFERENCES

1. S. Sinha, K. Natesan, and M. Blander, "A New Calculational Method for Deducing the Complex Chemistry of Coal Ash Deposits," Proceedings of the Conference on Mineral Matter and Ash Deposition from Coal, Santa Barbara, California, February 21-26, 1988, in press.
2. M. Blander, S. Sinha, A. Pelton, and G. Eriksson, "Calculations of the Chemistry of Coal Combustion Effluents," Proceedings American Flame Research Committee 1988 Fall Meeting, Pittsburgh, Pennsylvania, October 4-6, 1988, Paper No. 25.
3. J. E. Radway, "All You Ever Want to Know About Additive Application and Testing," Proceedings of the Conference on Mineral Matter and Ash Deposition from Coal, Santa Barbara, California, February 21-26, 1988, in press.
4. G. Eriksson, *Chemica Scripta*, **8**, 100-103 (1975).
5. W. T. Thompson, C. W. Bale, and A. D. Pelton, *F*A*C*T Users Guide*, McGill University, Ecole Polytechnique, Montreal (1988).
6. M. Blander and A. D. Pelton, "Computer Assisted Analysis of the Thermodynamic Properties of Slags in Coal Combustion Systems," ANL/FE-83-19, Argonne National Laboratory, Argonne IL (1983).
7. A. D. Pelton and M. Blander, *Metall. Trans.* **17B**, 805-815 (1986).
8. M. Blander and A. D. Pelton, *Geochim. et Cosmochim. Acta*, **51**, 85-95 (1987).

Table I. Composition of High-Sulfur Illinois #6 Coal Used for the Present Work

Coal Constituents		Ash Constituents	
Species	Wt %	Species	Wt %
C	60.15	SiO ₂	46.77
H	4.26	Fe ₂ O ₃	16.22
N	0.97	Al ₂ O ₃	18.47
S	3.41	CaO	6.91
Cl	0.05	MgO	1.28
H ₂ O	10.54	SO ₃	4.35
O	7.30	Na ₂ O	4.96
Ash	13.32	Unknown	1.04
TOTAL	100.00		100.00

Table II. Calculated Slag Compositions
(Weight Percent)

	Temperature (K)					
	1800	1700	1600	1500	1400	1300
<u>w/o CaCO₃</u>						
SiO ₂	57.47	65.63	74.63	77.27	78.62	78.08
FeO	23.57	16.15	7.41	1.92	0.32	0.06
CaO	10.27	6.65	3.61	2.22	1.03	0.51
Na ₂ O	7.07	9.43	11.71	15.81	18.98	20.87
MgO	1.63	2.13	2.64	2.79	1.04	0.48
wt (g)	9.78	7.45	6.02	4.46	3.72	3.38
<u>6.25 g CaCO₃ added</u>						
SiO ₂	42.16	44.11	45.90	46.65	47.56	71.27
FeO	19.41	9.86	4.63	1.88	0.64	0.06
CaO	31.46	36.40	38.48	40.13	34.97	4.49
Na ₂ O	5.63	7.85	8.97	9.26	13.74	23.91
MgO	1.34	1.80	2.03	2.09	3.10	0.27
wt (g)	11.87	8.85	7.84	7.62	5.14	0.16

Table III. Molten and Solid Sulfate Condensates
(Weight Percent)

	1350		1300		1250		1150		1050	
	Without CaCO ₃	With CaCO ₃	Without CaCO ₃	With CaCO ₃	Without CaCO ₃	With CaCO ₃	Without CaCO ₃	With CaCO ₃	Without CaCO ₃	With CaCO ₃
<u>Liquid</u>										
Na ₂ SO ₄	--	94.77	--	91.10	96.65	80.73	--	--	--	--
CaSO ₄	--	5.22	--	8.89	3.25	19.25	--	--	--	--
MgSO ₄	--	0.01	--	0.01	0.10	0.21	--	--	--	--
wt (g)	--	1.61	--	1.68	1.67	2.04	--	--	--	--
<u>Solid</u>										
Na ₂ SO ₄	--	--	--	--	--	--	50.29	45.78	50.32	49.58
CaSO ₄	--	--	--	--	--	--	49.47	54.11	44.72	48.88
MgSO ₄	--	--	--	--	--	--	0.25	0.12	4.96	1.54
wt (g)	--	--	--	--	--	--	3.22	3.53	3.22	3.26
<u>Solid</u>										
CaSO ₄	--	--	--	--	--	--	--	99.77	87.86	96.62
MgSO ₄	--	--	--	--	--	--	--	0.23	12.14	3.38
wt (g)	--	--	--	--	--	--	--	5.01	1.14	9.66

Table IV. Solid Condensates (in grams)

	w/o CaCO_3				w/ CaCO_3			
	1350	1250	1150	1050	1350	1250	1150	1050
$\text{CaAl}_2\text{Si}_2\text{O}_8$	4.85	4.87	1.73	--	7.16	7.16	7.16	--
Fe_2O_3	2.56	2.56	2.56	2.56	2.56	2.56	2.56	2.56
SiO_2	1.25	3.82	4.50	5.02	0.00	0.21	3.10	5.05
$\text{Al}_6\text{Si}_2\text{O}_{13}$	1.18	--	--	--	--	--	--	--
MgSiO_3	0.33	0.40	0.39	0.15	--	--	--	0.08
Al_2SiO_5	--	1.34	3.17	4.17	--	--	--	4.17
CaSiO_3	--	--	--	--	5.78	5.55	--	--
$\text{CaMg}(\text{SiO}_3)_2$	--	--	--	--	0.85	0.85	0.83	--

A PHYSICAL AND CHEMICAL BASIS FOR UNDERSTANDING INORGANIC MINERAL TRANSFORMATIONS IN COALS BASED ON MODEL-MINERAL EXPERIMENTS

S. Srinivasachar, J.J. Helble, and A.A. Boni
PSI Technology Company
Research Park, P.O.Box 3100
Andover, MA 01810

Abstract

Ash deposition depends on the size, surface composition and surface state of the transformed coal minerals. It is currently assumed that the minerals found in coals can be described in terms of their elemental chemical oxides. We hypothesize that each mineral represents a unique physico-chemical entity that undergoes a complex transformation as it is processed by the combustion environment and eventually reaches an oxidized state. We have performed drop-tube furnace experiments, with representative combustion conditions, on two important coal minerals: pyrite and illite. Comparison is made with an Eastern coal containing large quantities of the above minerals. There is evidence of exothermic and endothermic reactions, fragmentation, kinetic and transport-limited oxidation, and formation of both complex glasses and crystalline phases, at different stages in the mineral transformation process. These processes determine the final size, composition, and the surface state of the ash, which cannot be predicted by thermochemical methods alone.

INTRODUCTION

Ash deposition on heat transfer surfaces is the most severe problem associated with the combustion of coal. Besides lowering heat transfer rates, hence plant efficiencies, frequent maintenance and unscheduled shutdowns for removing these deposits substantially adds to the cost of power generation. It is therefore critical that for a given pulverized coal (p.c.) fired boiler, appropriate coals be selected and operating conditions be maintained to minimize ash deposition and its detrimental effects. Presently, empirical indices based on the elemental oxide composition are used to rank a coal's fireside behavior.^{1,2} These slagging and fouling "factors" are only applicable to very specific types of coal, coal ash and boiler units and extension of these factors to different coal/ash types or combustion conditions gives results which are uncertain at best. This can be attributed to the fact that different coals contain different amounts and species of minerals,³ and their specific physical and chemical transformations govern the state in which they arrive at a heat transfer surface and deposit. Slagging and fouling factors that are defined and used at present average out the expected behavior of the coal ash, i.e. they consider the coal and ash to be homogeneous and represented as a sum of individual elemental oxides. The detrimental deposition characteristics of ash resulting from some problematic individual minerals or their combinations is thus masked out. An understanding of the transformations of individual minerals in coal is therefore needed to develop a better predictor for ash deposition.

Iron and alkali-bearing minerals, for example, pyrite and illite respectively have long been recognized as a major source of wall slagging. The behavior of excluded pyrite particles under combustion conditions has been

reported by our group in detail previously^{4,5} and is only summarized here. The focus of this article is on transformations of illite under similar processing conditions. The stickiness characteristics of illite transformed in a combustion environment is also examined.

EXPERIMENTAL

All combustion and deposition experiments were performed in a resistance-heated entrained flow reactor, operated under laminar flow conditions. Schematics and detailed description of the reactor is given elsewhere⁶ and the deposit collection probe is shown in Figure 1. Samples of size-graded illite were entrained in an air stream and injected axially into the isothermal furnace via a water-cooled injector at a rate of about 0.3 gm/minute. Air was used as the furnace gas, and was injected separately through the top of the reactor. Gas temperature was held at 1500 K for the transformation experiments, but was varied for the stickiness determination experiments. For the former set of experiments, the particle residence time was varied from 0.8 to 2.5 seconds in the isothermal section, while it was held constant at 2.5 seconds for the stickiness tests.

The particles were collected via one of the following techniques:

1. isokinetic sampling, via a water-cooled, nitrogen-quenched probe. At the exit of the probe, all particles passed through a seven stage Pollution Systems Control Corp. cascade impactor, providing on-line size classification of all particles larger than 0.1 microns. Smaller particles were collected on a backup filter. In experiments where size classification was not required, a total filter was used.
2. deposition of a portion of the supermicron particles on a deposit collection probe. The capture efficiency is determined from the ratio of the mass of the deposit on the mullite tube to the mass of the particles that passed through the projected area of the substrate tubes. The gas temperatures at the deposition location, although intended to be the same as the furnace temperature, are 70 - 100 K lower.

Chemical Analysis of Illite

The illite examined in this study was a Cambrian shale from the Silver Hill formation, Jefferson Canyon, Montana. This illite has been characterized in detail by Hower et al.. The chemical composition (weight percent) of Silver Hill illite is as follows: SiO₂ (55.1), Al₂O₃ (22.0), K₂O (8.0), FeO (1.34),

Fe₂O₃ (5.3), MgO (2.8), Na₂O (0.08), H₂O- (1.0), H₂O+ (6.4). H₂O- represents the

weight loss at 110°C while H₂O+ is the weight loss on ignition. The composition of illite in various coals may be slightly different from each other, and therefore their behavior in the furnace may be somewhat different. One of the anticipated differences could be the fraction of the iron that is present in the ferrous state, as this will have significant impact on the its melting characteristics. However a study of Silver Hill illite can provide information as to the transformations undergone by "generic" illite in the combustion zone.

RESULTS AND DISCUSSION

Transformations of Illite

Samples of illite in the size range of 53 to 75 microns, exposed to high temperatures in the reactor for different residence times were examined by scanning electron microscopy (Figure 2). Illite particles in the feed are angular with an aspect ratio of about 1.5 to 2.0 for most particles. Upon exposure to 1500 K for a residence time of approximately 0.9 seconds, the color of the sample changed from a greenish gray to dark brown reflecting the oxidation of iron to the ferric state. Particles lose their angular form partially (Figure 2b) and vitrification is evident, although the overall morphology still resembles that of the original particle. Also isolated pore formation and gas evolution through these pores is evident. Examination of particles subjected to 1500 K for 2.5 seconds, shows that a much larger fraction had completely molten (Figure 2c). Several large pores are present on the particle surface, suggesting gas evolution and even some bloating as a result of trapped vapor trying to escape through a molten matrix. Gas evolution during heating consists of the release of the chemically bound hydroxyl groups. At slow heating rates, dehydroxylation does not occur until 600-700°C. At the high heating rates in our experiments, even higher particle temperatures would be reached before this step occurs. This endothermic step further delays the breakdown of the illite structure and its transformation into a glass.

The equilibrium behavior of illite can be determined from the $K_2O-Al_2O_3-SiO_2$ phase diagram. The phase diagram (Figure 3) shows that the minimum melting point appropriate to illite composition is 985°C. With addition of MgO and other components (particularly FeO, Fe_2O_3), a much lower eutectic melting point would be expected. The behavior of illite during the firing of ceramics was studied by Segnit and Anderson in an electric muffle furnace at heating rates of 100°C per hour and a soaking time of 4 hours. Clearly under these conditions one would be closer to equilibrium than in our experiments. They determined that glass formation started at 850°C, and vitrification was complete at 1000°C. Some pore formation was seen at 1050°C, and much more bloating and pore opening was evident at 1100°C. A comparison of the equilibrium behavior and the Segnit and Anderson work with our results shows that the transformations of illite under p.c. firing conditions would not approach the equilibrium condition, either during the heat-up stage or while cooling, for example when approaching a heat transfer surface after combustion has been completed. One would expect that under actual combustion temperatures which are higher than in our experiments (1500°C), and given that illite is associated with the coal during combustion (hence, even higher particle temperatures), illite will be completely molten before it arrives at a deposition surface. It then becomes important to describe the phase change kinetics and their impact on viscosity as the ash particle cools down. This transient viscosity variation will determine the deposition potential of the incoming ash particles.

Composition analysis of the raw and transformed illite particles was performed to determine if there was any preferential movement of potassium or iron to the particle surface. Surface analyses proved inconclusive since there was considerable compositional variation between different particles. A clearer picture of the selective mobilization of specific elements can only be obtained

by analyzing the particle cross-sections. We intend to do this as a next step. We also determined size distribution of the burnt illite particles using the cascade impactor. Data showed that all the particles were collected on the top stage of the impactor ($d_p > 8$ microns). This means that there is no vaporization of the illite (especially of the potassium) when it is not associated with carbon, nor any fragmentation into the 1 - 5 micron size range. Association with carbon would only mean that it would melt more quickly, thus impeding any fragmentation, although the higher temperatures might cause some vaporization.

Stickiness Behavior

Capture efficiencies of transformed illite particles were determined in the manner described in the experimental section. The capture efficiency is the fraction of the particles that both impact and stick. Impaction efficiency is determined from Stokes number considerations, and for the particle size (53-75 microns) and the velocity range used here, the impaction efficiency is unity. Figure 4 shows the capture efficiencies for different furnace temperatures and particle impaction velocities. When examined as a function of temperature, there is a dramatic increase in the rates of capture above 1400 K, except for the highest velocity. As the temperature is increased, the viscosity of the incoming particles decrease, and below a critical viscosity (approximately 10^7 poise) the particles are sufficiently deformable that the energy of impact is dissipated, and the particles stick without rebounding. One would normally expect that the capture efficiency would increase as the particle velocity increases - however, in our case the particles are large enough that all of them impact even at the lowest velocity. The observed reduction in the capture efficiency with increasing velocity must therefore be due to deposit erosion from the incoming particles. Microscopic observation of the deposit also showed that it was bonded at the higher temperatures, whereas at 1400 K, even though the capture efficiencies were high, the deposit was powdery and very friable. Quantitative analysis of these data will require consideration of both deposition and erosion.

Comparison of Illite and Pyrite Transformations

In a previous study,^{4,5} the transformations of pyrite were examined in the same entrained flow reactor setup. A comparison shows that the physical and chemical changes associated with the oxidation of pyrite is much more complex than for illite. Pyrite decomposed to pyrrhotite ($\text{Fe}_{0.877}\text{S}$), and this was followed by its oxidation to a molten sulfide-oxide mixture, subsequent crystallization of magnetite (Fe_3O_4) from the melt, and finally formation of hematite (Fe_2O_3). Particle temperature exceeds the gas temperature during this process due to the exothermic oxidation of sulfide. There was also a residence time region in which the particle remained molten. This constituted 80 percent of the total time for oxidation to magnetite. But, once magnetite formation was completed, the particle solidified, so that deposition was favored only as long as the pyrite was partially oxidized. Illite, on the other hand, does not exhibit such dramatic changes upon heating. Once the illite particle is molten, it is expected to remain as such until the gas, hence particle, temperature is lowered. Besides the formation of glass, the predominant reaction for illite seems to be the loss of the hydroxyl group, an endothermic reaction. Further analysis by EXAFS and Mossbauer techniques would reveal how the chemical

structure of iron and potassium in the illite-derived glass changes.

Based on limited data on the behavior of the minerals in coal,¹¹ the similarity with the behavior of the pure minerals is borne out. In Kentucky #11 coal, where the minerals are finely and uniformly dispersed through the coal matrix, examination of the ash size distribution showed that a large degree of coalescence was taking place. The final ash composition showed glasses with compositions ranging between illite, kaolinite, and silica, suggesting that the molten illite had incorporated the other minerals within its matrix. This data are also not inconsistent with little fragmentation seen with pure illite and that illite is expected to melt under combustion conditions. Mossbauer data on iron showed that only a small portion of the iron was in a glass, and the level of iron present as hematite increased as the oxygen level in the gas was raised.⁴ This is consistent with model calculations for oxidation of the pure mineral.

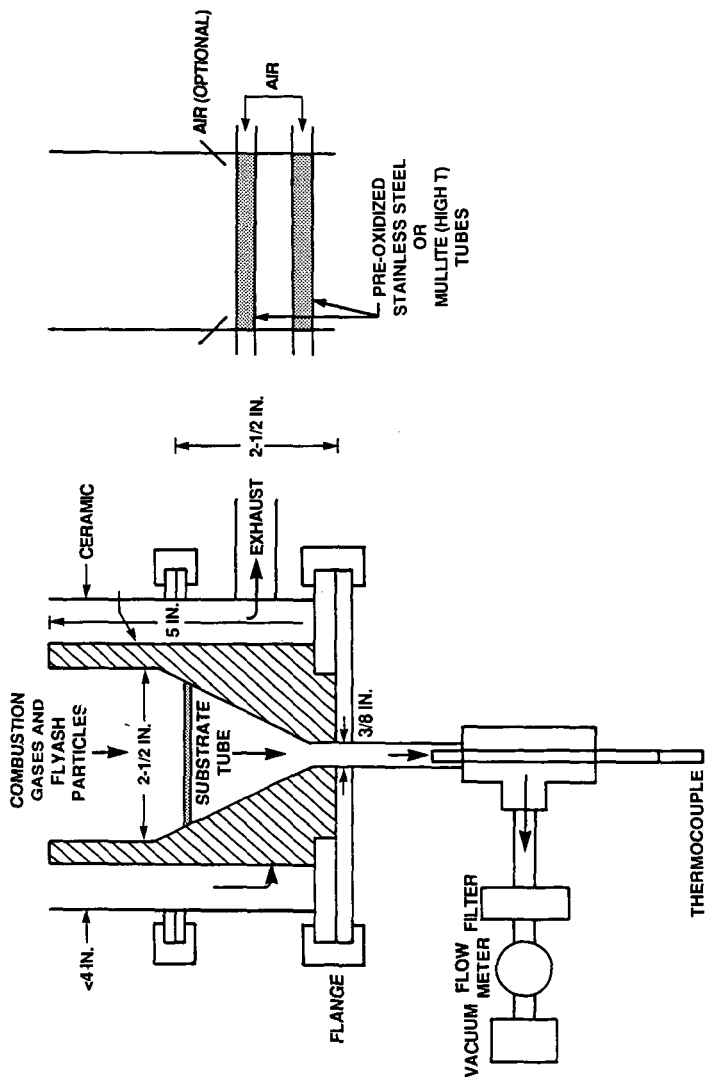
ACKNOWLEDGEMENTS

The authors thank the Department of Energy, Pittsburgh Energy Technology Centre for their support of this work under Contract No. DE-AC22-86PC90751

REFERENCES

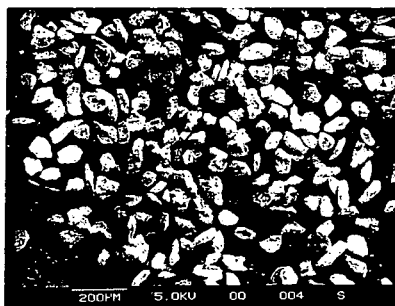
1. Winegartner, E.C., Coal Fouling and Slagging Parameters, American Society of Mechanical Engineers (1974).
2. Bryers, R.W., "An Overview of Slagging/Fouling Due to Impurities in Coal," Proceedings of EPRI Conference on Effects of Coal Quality on Power Plants, October (1987).
3. Boni, A.A., Flagan, R.C., Bryers, R.W., Sarofim, A.F., Beer, J.M., Peterson, T.W., Wendt, J.O.L., Huffman, G.P., Huggins, F.E., Helble, J.J., Srinivasachar, S., "Transformations of Inorganic Coal Constituents in Combustion Systems," Proceedings of DOE AR&TD Meeting, (1987).
4. Srinivasachar, S., and Boni, A.A., "A Kinetic Model for Pyrite Transformations in a Combustion Environment," Fuel (accepted) (1988).
5. Srinivasachar, S., Helble, J.J., Katz, C.B., Morency, J.R., and Boni, A.A., "Experimental and Modeling Study of Pyrite Transformations under Coal Combustion Conditions," Coal: Fuel for Today and for the Future, International Symposium, American Flame Research Committee, October (1988).
6. PSI Technology Company, "Transformations of Inorganic Coal Constituents in Combustion Systems," Quarterly Report No. 2, DOE Contract DE-AC22-86PC90751, April (1987).
7. Hower, J., and Mowatt, T.C., *Amer. Mineralogist* **51**, 825 (1966).
8. Levin, E.M., Robbins, C.R., and McMurdie, H.F., Phase Diagrams for Ceramists, The American Ceramic Society (1964).
9. Segnit, E.R., and Anderson, C.A., *Trans. Br. Ceram. Soc.* **71**, 85 (1972).
10. Srinivasachar, S., Helble, J.J., Katz, C.B., and Boni, A.A., "Transformations and Stickiness of Minerals During Pulverized Coal Combustion," Proceedings of the Engineering Foundation Conference on Mineral Matter and Ash Deposition in Coal (in press) (1988).
11. Helble, J.J., Srinivasachar, S., Katz, C.B., and Boni, A.A., "Mineral Transformations in Selected Coals-Size and Composition of the Ash", ACS Meeting, Dallas (to be presented) (1989)

STICKY PROBE

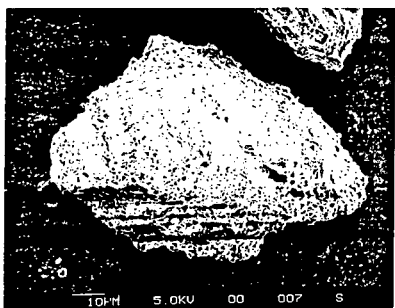


A-7398

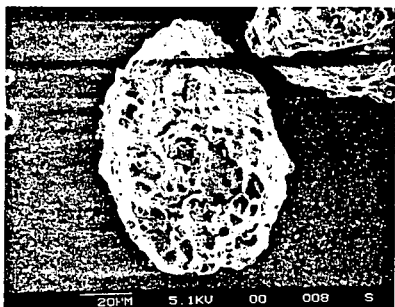
Figure 1. Schematic of the deposit collection probe



a)



b) Res. time ~0.9 seconds



c) Res. time ~2.5 seconds

Figure 2. Scanning Electron Micrographs of a) raw and b), c) Burnt Illite at Different Residence Times ($T_{\text{gas}} = 1500\text{K}$) for 53-75 Micron Particle Size Fraction

$K_2O-Al_2O_3-SiO_2$

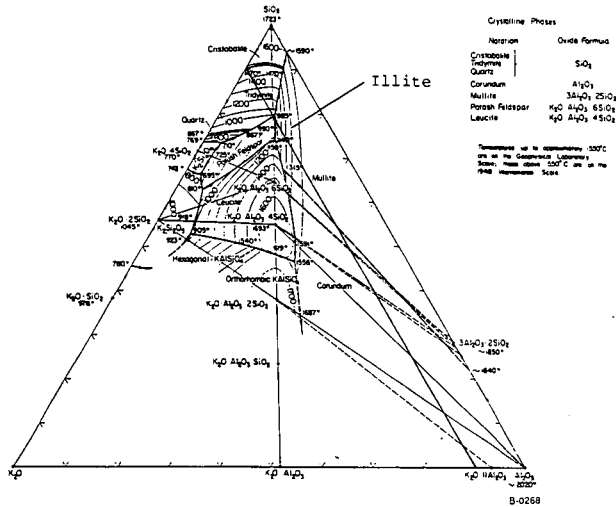


Figure 3. System $K_2O-Al_2O_3-SiO_2$; Composite. E.F. Osborn and Arnulf Muan, Revised and Redrawn "Phase Equilibrium Diagrams of Oxide Systems," Plate 5, Published by the American Ceramic Society and the Edward Orton Jr., Ceramic Foundation, 1960.

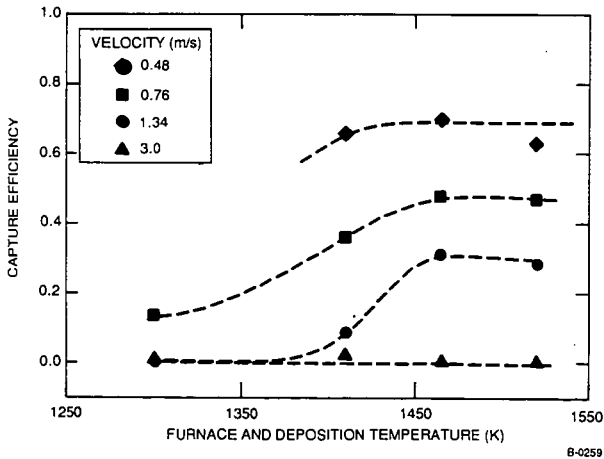


Figure 4. Capture Efficiencies (slagging probe) for Burnt Illite at Different Furnace Temperature and Particle Impaction Velocities